J. Fluid Mech. (2014), *vol.* 743, *pp.* 606–635.
doi:10.1017/jfm.2014.40

Spanwise oscillatory wall motion in channel flow: drag-reduction mechanisms inferred from DNS-predicted phase-wise property variations at $Re_\tau = 1000$

L. Agostini[1,†], E. Touber[2] and M. A. Leschziner[1]

[1]Department of Aeronautics, Imperial College London, South Kensington Campus, London SW7 2AZ, UK

[2]Department of Mechanical Engineering, Imperial College London, South Kensington Campus, London SW7 2AZ, UK

(Received 24 April 2013; revised 16 December 2013; accepted 14 January 2014; first published online 10 March 2014)

A direct-numerical-simulation-based study is presented, which focuses on the response of near-wall turbulence and skin friction to the imposition of an oscillatory spanwise wall motion in channel flow. One point of contrast to earlier studies is the relatively high Reynolds number of the flow, namely $Re_\tau = 1000$ in the unforced baseline flow. Another is the focus on transients in the drag that are in the form of moderate oscillatory variations in the skin friction and near-wall turbulence around the low-drag state at a sub-optimal actuation period. These conditions allow phase-averaged statistics to be extracted, during the periodic drag decrease and rise, that shed light on the interaction between turbulence and the unsteady Stokes strain. Results are presented for, among others, the phase-averaged second moments of stochastic fluctuations and their budgets, enstrophy components and joint probability density functions. The study identifies velocity skewness – the wall-normal derivative of the angle of the velocity vector – as playing a significant role in the streak-damping process during the drag-reduction phase. Furthermore, the phase-wise asymmetry in the skewness is identified as the source of a distinctive hysteresis in all properties, wherein the drag decrease progresses over a longer proportion of the actuation cycle than the drag increase. This feature, coupled with the fact that the streak-generation time scale limits the ability of the streaks to re-establish themselves during the low-skewness phase when the actuation period is sufficiently short, is proposed to drive the drag-reduction process. The observations in the study thus augment a previously identified mechanism proposed by two of the present authors, in which the drag-reduction process was linked to the rate of change in the Stokes strain in the upper region of the viscous sublayer where the streaks are strongest. Furthermore, an examination of the stochastic-stress budgets and the enstrophy lead to conclusions contrasting with those recently proposed by other authors, according to which the drag-reduction process is linked to increases in enstrophy and turbulence-energy dissipation. It is shown, both for the transient drag-reduction phase and the periodic

† Email address for correspondence: l.agostini@imperial.ac.uk

drag fluctuations around the low-drag state, that the drag decrease/increase phases are correlated with decreases/increases in both enstrophy and dissipation.

Key words: drag reduction, turbulence control, turbulent boundary layers

1. Introduction

Several recent computational and experimental studies, both for channel flow (e.g. Quadrio & Ricco 2004; Ricco & Quadrio 2008; Quadrio, Ricco & Viotti 2009; Touber & Leschziner 2012) and for spatially evolving boundary layers (e.g. Choi 2002; Di Cicca *et al.* 2002; Ricco 2004; Yudhistira & Skote 2011; Lardeau & Leschziner 2013; Skote 2013) demonstrate that the imposition of spanwise oscillatory wall motion onto a streamwise turbulent near-wall layer results in a substantial decrease in skin friction if the wall-velocity amplitude and oscillation period are chosen judiciously. In the case of streamwise-homogeneous wall motion, the skin friction drops by a maximum of around 35 % at the friction Reynolds number $Re_\tau = O(200)$, a wall-velocity amplitude $W_m{}^+ = W_m/u_\tau = 12$ (u_τ is the friction velocity) and oscillation period $T^+ = Tu_\tau^2/\nu \approx 100$ (ν is the kinematic fluid viscosity), but this margin appears to decrease roughly in proportion to $Re_\tau^{-0.2}$ ($Re_\tau = u_\tau h/\nu$; h is the channel half-height), a rate based on simulations by Touber & Leschziner (2012) at $Re_\tau = 500$ and 1000. Quadrio *et al.* (2009) show that higher margins – around 45 % at $Re_\tau = O(200)$ – can be achieved if the wall motion is imposed in the form of streamwise stationary or travelling waves. More importantly, from a practical perspective, is the fact that this actuation mode results in a material energetic net gain, when the expenditure of actuation power is accounted for.

One broadly consistent observation that emerges from most channel-flow studies is that the optimum oscillation period is $T^+ \approx 100$, although in the case of spatially-evolving boundary layers, there is some evidence (Ricco 2004; Skote 2011, 2012; Lardeau & Leschziner 2013) that the optimum value is somewhat lower, closer to 70. At the optimum period, the drag reduces, following a transient phase observed to be around three oscillation periods, to a low-drag state (in a time-averaged sense), which is characterized by insignificant periodic fluctuations associated with the actuation time scale. At this condition, the Stokes layer – the unsteady transverse shear layer generated by the wall motion – is confined to the viscous sublayer ($y^+ < 15$), and the quasi-organized near-wall streaks, primarily associated with the turbulent skin friction, are observed to be especially weak and to be almost unaffected by the unsteady motion. Linear analysis by Blesbois *et al.* (2013), based on the general optimum perturbation (GOP) theory, suggests that this insensitivity is associated with the fact that streak amplification, following their destruction through effects of the unsteady Stokes strain (the wall-normal gradient of the spanwise velocity) at $T^+ = 100$–200, is subject to a time scale $t^+ = O(80)$. Hence, it may be inferred that if the proportion of the actuation period during which the strain field allows the streaks to re-establish is too short, the streaks never fully recover and the drag remains low. As the oscillation period increases, the Stokes layer penetrates into the turbulent buffer layer, and the Stokes strain in the viscous sublayer decreases. This, in combination with the increased actuation time scale, relative to the streak-generation time scale, degrades the drag-reduction effectiveness, and one feature accompanying this degradation is the appearance of distinct oscillatory variations of the skin friction and turbulence properties around the low-drag state.

From the point of view of studying the drag-reduction mechanisms, non-optimal actuation offers the opportunity to probe the pertinent fundamental interactions through a scrutiny of phase-averaged turbulence properties during phases of drag increase and decrease within any actuation period. Touber & Leschziner (2012) show that, at $Re_\tau = 500$ and $T^+ = 200$, these oscillations are accompanied by distinctive variations in the structure of the near-wall streaks. Thus, the streaks are observed to weaken and strengthen twice during any one actuation cycle, with the weakening associated with phases of low values of and rapid change in the Stokes strain and its direction, and strengthening with high values of and slow phase-wise change in the strain. Moreover, the streak orientation is close to bimodal, the angle being dictated by the direction of the shear-strain vector in the viscous sublayer at phases at which the Stokes strain is high and lingers in terms of both strength and direction. In contrast, the streaks are neither pronounced nor have a clear direction at phases in which the strain vector changes rapidly.

The above observations, supplemented by an analysis of streak-conditional phase-averaged data, presented by Touber & Leschziner (2012), and the linear analysis by Blesbois *et al.* (2013), go some way towards explaining certain physical mechanisms underpinning the drag-reduction phenomenon. However, the observations do not fully explain the precise fundamental nature of the interactions by which the unsteady Stokes motion depresses turbulence and drag, and there continues to be a lively debate about the mechanisms at play. This paper is intended to be a contribution to the debate.

One route taken in past efforts towards explaining what drives the drag towards a low time-averaged level has been to observe the transient behaviour of the flow properties following the sudden imposition of the spanwise oscillations onto the unforced baseline flow. Channel-flow studies by Quadrio & Ricco (2003) and Xu & Huang (2005) have adopted this route and have revealed that the drag and turbulence intensity reduce in a non-monotonic fashion, with turbulence production experiencing overshoots, especially during the initial portion of the transient path towards the low-drag state, the final level being attained within about three oscillation periods. A more recent study by Ricco *et al.* (2012) considers specifically the relationship between enstrophy and dissipation in the transient period. The authors argue, based on direct numerical simulation (DNS) studies of the transient response of the drag at $Re_\tau = 200$, that the key mechanism is an increase in the enstrophy, provoked by the Stokes strain, and hence an associated rise in the turbulence dissipation, which then causes turbulence and drag to decrease.

Whether Ricco *et al.* (2012)'s paradigm is supported by the present observations is one issue that is addressed in this paper as part of an analysis of data derived from direct numerical simulations at $Re_\tau = 1000$ for the unforced baseline flow, the bulk Reynolds number being approximately 2×10^4, based on half-channel height. In contrast to earlier studies, the emphasis is on the periodically time-varying phase-averaged fields of stochastic properties, with periodicity provoked by actuation at the non-optimal period $T^+ = 200$. This approach is preferred to one that examines the transient phase for three main reasons: it allows the stochastic turbulence to be unambiguously separated from the transient motions; it avoids uncertainties arising from an incomplete penetration of the Stokes motion through the viscous sublayer during the transient period; and it permits the analysis and conclusions to rest on a much larger statistical sample, which is extracted from 20 fields per phase value (at $T^+ = 200$), rather than a single field per time level in the transient analysis. This third issue is especially important at the much higher Reynolds number examined here,

relative to earlier studies, in which case the use of a single field per time level results in statistically ill-converged results for some properties, for example turbulence-energy dissipation and higher-order stress-budget contributions. In order to demonstrate the equivalence between the transient and phase-averaged processes, notwithstanding the stated limitations on capturing the latter reliably, the paper includes a juxtaposition of analogous variations for the streamwise Reynolds stress, the dissipation and enstrophy. These provide a strong indication that the processes linking the phase-averaged drag decrease to the stochastic turbulence fields during the periodic drag oscillations around the low-drag state are the same as those operating during the transient phase.

2. Computational conditions

All simulations reported herein have been performed with a variant of the general non-orthogonal-grid, block-structured, finite-volume method based on a fully collocated storage and realized in the in-house code STREAM-LES, initially developed by Temmerman *et al.* (2003) for incompressible flows. The algorithm advances the velocity field in time by means of a fractional-step method incorporating fourth-order approximations for the convective and diffusive fluxes and a third-order Gear-like scheme documented in Fishpool & Leschziner (2009), shown to possess advantageous stability and accuracy properties, relative to a corresponding second-order time-advancement scheme. Zero divergence is secured by solving the pressure-Poisson equation with second-order accuracy, combining the application of an implicit successive over-relaxation (SLOR) method with a multigrid scheme. Pressure–velocity decoupling, arising from the fully collocated storage of velocity and pressure, is counteracted by employing the so-called Rhie & Chow (1983) interpolation scheme. Fishpool & Leschziner (2009) demonstrate that the loss of energy due to artificial dissipation arising from the Rhie & Chow interpolation is low. The code is fully parallelized using MPI, with pre-determined grid blocks or sub-domains assigned to individual processors.

The actuation under consideration is restricted to a purely sinusoidal spanwise oscillation of the wall, namely:

$$W(t) = W_m \sin(2\pi t/T). \tag{2.1}$$

In the present study, $W_m{}^+ = W_m/u_\tau = 12$ and $T^+ = Tu_\tau{}^2/\nu = 100$ or 200. These values are the same as those used by Touber & Leschziner (2012) at $Re_\tau = 500$ as well as others reporting DNS studies investigating drag-reduction phenomena in channel flow at lower Re_τ values. As pointed out earlier, $T^+ = 100$ is close to the optimum actuation period in channel flow within the range of Reynolds number investigated so far. However, given this T^+ value, the maximum drag-reduction margin is materially sensitive to $W_m{}^+$, varying between 22 % and 39 % within the range $W_m{}^+ = 6$–18 at $Re_\tau = 200$ (Quadrio & Ricco 2004). This dependence is of subordinate importance, however, in the context of the present primary objective of studying the periodic fluctuations of drag and turbulence properties in non-optimal conditions.

All simulations were performed over the same box of length, height and depth $4\pi h \times 2h \times 2\pi h$, respectively, corresponding to approximately $12 \times 2 \times 6 \times 10^3$ wall units. The box was covered by $1056 \times 528 \times 1056\,(= 589 \times 10^6)$ nodes. The corresponding cell dimensions were Δx^+, $\Delta y^+{}_{min}$, $\Delta y^+{}_{max}$, $\Delta z^+ = 12.2$, 0.4, 7.2, 6.1. These normalized values arise upon the use of the actual (rather than the nominal) friction Reynolds number for the unactuated flow, namely $Re_\tau = 1025$. All simulations are performed at a constant time-marching step $\Delta t^+ = 0.125$, chosen such that the

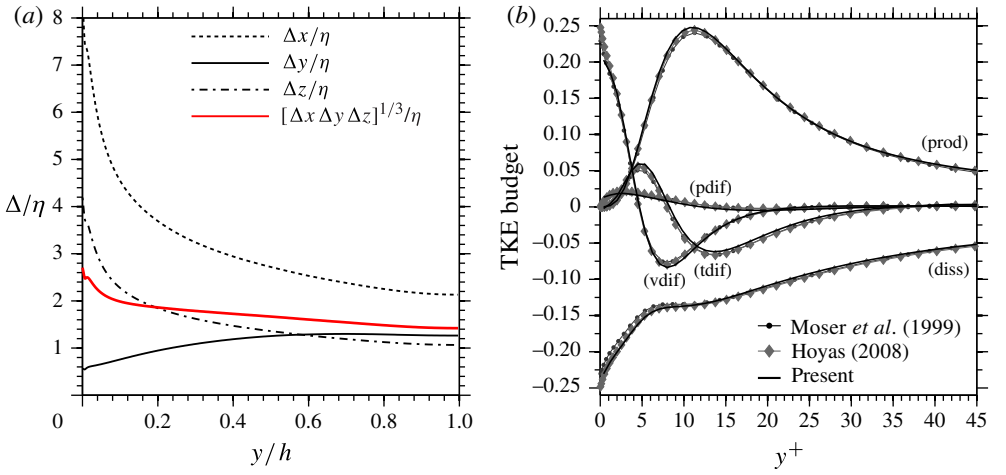

FIGURE 1. (Colour online) Resolution indicators: (*a*) comparison of cell dimensions relative to the Kolmogorov length scale; (*b*) turbulence-energy budget at $Re_\tau = 1000$ relative to that of Moser *et al.* (1999) at $Re_\tau = 590$ and Hoyas & Jiménez (2008) at $Re_\tau = 950$ for the baseline channel flow ('prod'= production, 'diss' = dissipation, 'tdiff' = turbulent diffusion, 'vdiff = viscous diffusion, 'pdif' = pressure diffusion).

CFL number, based on the maximum streamwise velocity, did not exceed 0.25. In the actuated flows, data were collected over a period $t^+ = 4600$ (about 7 flow-through times), corresponding to 46 and 23 actuation periods $T^+ = 100$ and 200, respectively. The statistical averaging exploited both spanwise and streamwise homogeneity, as well as the symmetry about the channel centreplane. Given the relatively low number of actuation cycles covered at $T^+ = 200$, the statistical convergence of phase-averaged quantities requires clarification. This will be done ahead of the presentation of phase-averaged results in § 3.2.5.

The adequacy of the resolution was investigated in various ways, including a simulation of the unactuated flow over a grid of 1.2 billion cells, an examination of the resolved dissipation, relative to the imbalance of other terms in the turbulence-energy budget, and an evaluation of the ratio of cell distances to the Kolmogorov length scale. Figure 1(*b*) compares the present turbulence-energy budget for the baseline flow with two published sets of DNS data: one by Moser, Kim & Mansour (1999) at $Re_\tau = 590$ and the other by Hoyas & Jiménez (2008) at $Re_\tau = 950$. Figure 1(*a*) shows that the cell length scale, identified by the cubic root of the cell dimensions, is around twice the Kolmogorov scale across the entire channel. This resolution is comparable to that in many other published DNS studies.

3. Results

3.1. *Mean-flow characteristics*

The emphasis of this paper is squarely on the phase-averaged properties and on related interpretations. However, it is informative to precede this with a consideration of a narrow selection of time-averaged data that convey an overall picture of the actuated flows, relative to the baseline state. Another argument for including these data is that they pertain to the highest Reynolds number reported so far. This is a pertinent point as one of the most intensively debated questions in the area of turbulent

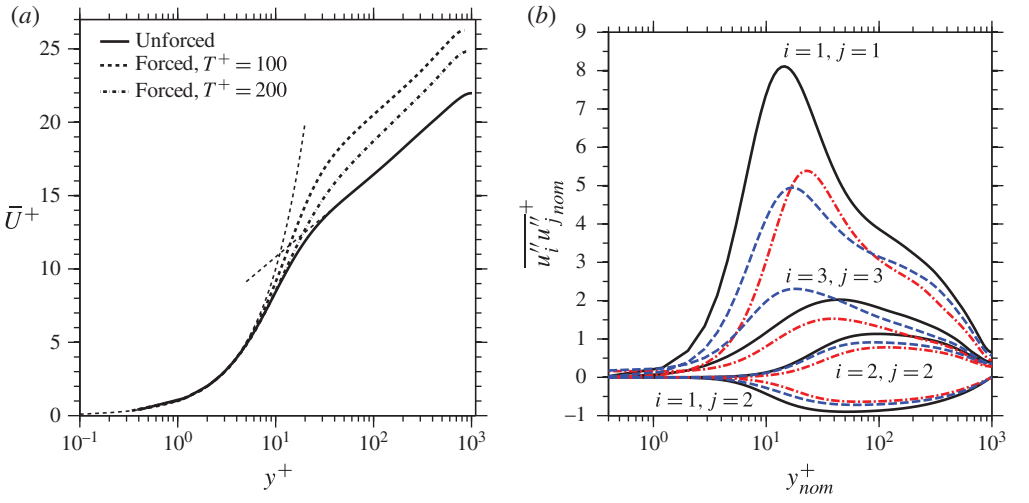

FIGURE 2. (Colour online) Profiles of (*a*) time-averaged logarithmic velocity profiles, scaled with the actual wall-shear stress; (*b*) time-averaged Reynolds stresses, scaled with baseline (nominal) wall-shear stress. In (*b*) dashed lines identify $T^+ = 200$; chain lines identify $T^+ = 100$; solid lines identify baseline flow; double-primes indicate stochastic fluctuations, as defined in (3.1).

drag reduction is the Reynolds-number dependence of the drag-reduction margin and its roots. The only result derived from the present study that was previously reported in Touber & Leschziner (2012) is the maximum drag-reduction margin at the near-optimum actuation period $T^+ = 100$, namely, 29 %, relative to 32 % at $Re_\tau = 500$ and 38 % at $Re_\tau = 200$, suggesting a decrease in the drag-reduction effectiveness roughly in accord with $Re_\tau^{-0.2}$. Results derived for $Re_\tau = 1000$ relate to a wide variety of properties and include full second-moment budgets for all stress components. The budgets, in particular, show characteristics that follow, certainly in qualitative terms, those that are discussed extensively by Touber & Leschziner (2012) at $Re_\tau = 500$, and they are not, therefore, included herein. On the other hand, phase-averaged budgets for $T^+ = 200$ are included in § 3.2, and these also give a good impression of the time-averaged behaviour at that actuation period, because the phase-averaged variations around the mean are not large.

Figure 2 shows time-averaged logarithmic velocity profiles, scaled with the actual wall-shear stress, and profiles of the normal Reynolds stresses, scaled with the nominal wall-shear stress (i.e. that of the unactuated flow). In the latter, and in other figures to follow, the double-primes indicate that the turbulence correlations are formed with the stochastic fluctuations. These arise from the decomposition:

$$U = \widetilde{U} + u'' = \overline{U} + \widehat{u} + u'', \tag{3.1}$$

where $\overline{U}$ is the time-averaged value, $\widetilde{U}$ is the phase-averaged value, evaluated from

$$\widetilde{U}|_\varphi = \frac{1}{N}\sum_{n=1}^{N}\left(\frac{1}{IK}\sum_{i,k=1,1}^{I,K} U_{i,k}|_{\varphi+(n-1)T}\right), \tag{3.2}$$

with $\varphi \in \{0, T\}$, i, k are x, z grid indices, N is the number of cycles over which averaging is performed, $\widehat{u}$ is the periodic fluctuation and u'' is the stochastic (purely

turbulent) contribution. The use of nominal scaling for the Reynolds stresses is deliberate, because it brings out, essentially, the absolute response of the turbulence to the actuation for the given bulk Reynolds number. In contrast, scaling with the actual friction velocity would be indicative of the degree of universality of the wall-scaled stresses; although this is an important issue, it is not one that is of principal interest in the present considerations.

Qualitatively, the response of the mean velocity and the stresses is similar to that reported and discussed extensively by Touber & Leschziner (2012) for $Re_\tau = 500$, but the magnitude of the response to the actuation is somewhat lower, reflecting the lower drag-reduction margins. Major points deserving to be highlighted are:

(i) the elevation of the log-law caused by a thickening of the viscous sublayer by approximately 5 wall units at $T^+ = 100$;

(ii) the large reduction in the streamwise stress (up to 40 % in the peak), especially in the lower parts of the viscous sublayer, indicative of the strong reduction in streak intensity;

(iii) the decrease in the maximum wall-normal stress and shear stress by around 30 % – this level scaling closely with the decrease in skin friction, and anticipated in view of the role played by the wall-normal stress in the shear-stress production rate;

(iv) the elevated value of the spanwise stress at $T^+ = 200$, exceeding the baseline level, and reflecting the consequences of the penetration of the Stokes layer into the turbulent region above the viscous sublayer and thus increasing the Stokes-strain-driven production $P_{\overline{w''w''}^+} = -2\overline{\widetilde{w''v''}\partial\widetilde{W}/\partial y}^+$, where the tilde identifies phase-averaging and the double-prime identifies stochastic fluctuations (see (3.1));

(v) the non-zero level of the spanwise normal stress at the wall, reflecting the difficulty of extracting the low stochastic near-wall component of the stress as the difference between the very large total and periodic components that prevail close to the wall; and

(vi) the lower peak of the streamwise stress at $T^+ = 200$ relative to that at $T^+ = 100$, associated with the periodic tilting of the streaks and their amplification at the phase in which tilting is strongest (see discussion by Touber & Leschziner 2012).

An additional point that deserves to be emphasized is that the spanwise stress at $T^+ = 100$ is lower than the baseline level, despite the additional production term $P_{\overline{w''w''}^+}$ that drives the spanwise normal stress. At the near-optimum actuation period, this term is very small, and the stress level is dictated by the pressure–strain process that transfers energy from the streamwise normal stress to the spanwise component. In contrast, at $T^+ = 200$, this extra generation is significant. As will be shown in § 3.2.5, the phase-averaged production $P_{\widetilde{w''w''}^+}$ varies substantially during the actuation cycle, between a mildly negative value to a maximum of around 65 % of the maximum streamwise-stress production ($P_{\widetilde{u''u''}^+} = -2\widetilde{u''v''}\partial\widetilde{U}/\partial y^+$). As a consequence, the time-averaged magnitude of the spanwise-stress production is around 30 % of that of the streamwise stress.

Figure 3 compares joint u''–v'' probability density functions (PDFs) for $T^+ = 100$ and the baseline flow, both at $y^+ = 13.5$. The choice of this particular value of the wall distance is rooted in the fact, as conveyed in figure 2, that this is the location around which the streamwise turbulence intensity (i.e. the streak strength) reaches its maximum value in the unactuated flow, and at which the actuation has the most

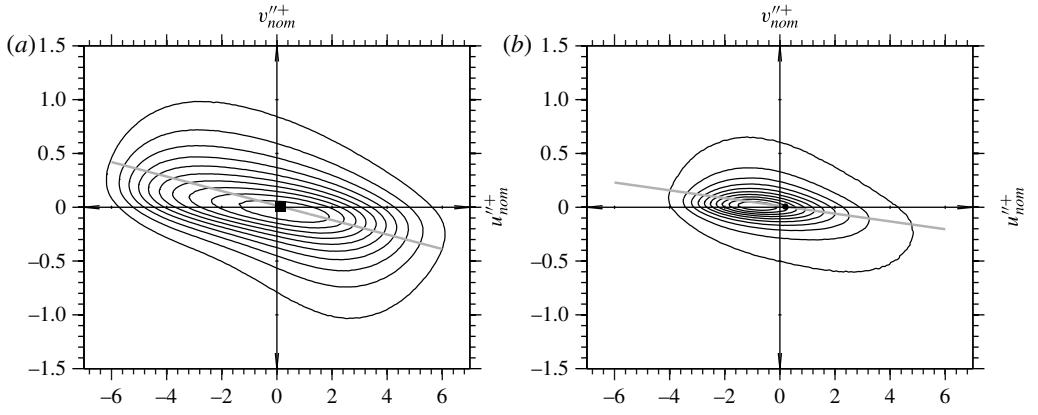

FIGURE 3. Joint u''–v'' PDFs at $y^+ = 13.5$ (*a*) for the baseline flow and (*b*) for the actuated flow at $T^+ = 100$.

pronounced effect on that intensity. The straight lines in the plots identify the principal axes of the PDFs, in a least-squares sense, determined from a scatter plot of all u''–v'' realizations recorded. The comparison reveals three main differences provoked by the actuation. First, as expected, there is a strong narrowing when actuation is imposed. Second, the reduction is more pronounced in the Q_2 quadrant ($u'' < 0$, $v'' > 0$) than in the Q_4 quadrant ($u'' > 0$, $v'' < 0$), indicating that the diminution of ejection intensity is more influential than that of sweeps. Third, there is a marked anticlockwise tilt in the PDF axis, indicative of a reduced level of cross-correlation between u'' and v'' fluctuations.

Finally, in this section, figure 4 shows the response of wall-normal and spanwise components of the enstrophy to the actuation at $T^+ = 100$. The streamwise component is relatively weak, and is also observed to be rather insensitive to the actuation, due to the fact that gradients of the streak strength – the intensity of the streamwise fluctuations – do not contribute directly to the streamwise component. The actuation is seen to result in a dramatic reduction in the other two components, reflecting the weakening of the streaks and their spanwise and wall-normal gradients. The reduction in the wall-normal component is accentuated by the decrease, albeit modest, in the spanwise-velocity fluctuations, reflected by the reduced level of the spanwise stress, as shown in figure 2. The spanwise enstrophy component is also very sensitive to the streak strength, being dependent on wall-normal gradients of the streamwise fluctuations. Hence, its decrease also reflects the weakening of the streaks. Clearly, however, the detailed responses of the two enstrophy components to the actuation differ greatly from each other. The wall-normal component has a maximum at around $y^+ \approx 13.5$, and this signifies the major contribution the streaky structures make to the wall-normal vorticity fluctuations. Its low magnitude, relative to the spanwise component, reflects the relatively large spanwise distances separating neighbouring streaks. In contrast, the strong near-wall maximum of the spanwise enstrophy component, in the baseline flow, is qualitatively consistent with the maximum of turbulence-dissipation rate observed at the wall, and is associated with the rise in the wall-normal derivative of the wall-parallel velocity fluctuations as the eddies 'flatten' in consonance with the approach to the two-component state at the wall. Its severe reduction by the actuation is partly a consequence of the strong damping in the streamwise fluctuations and their production across the lower part of the viscous

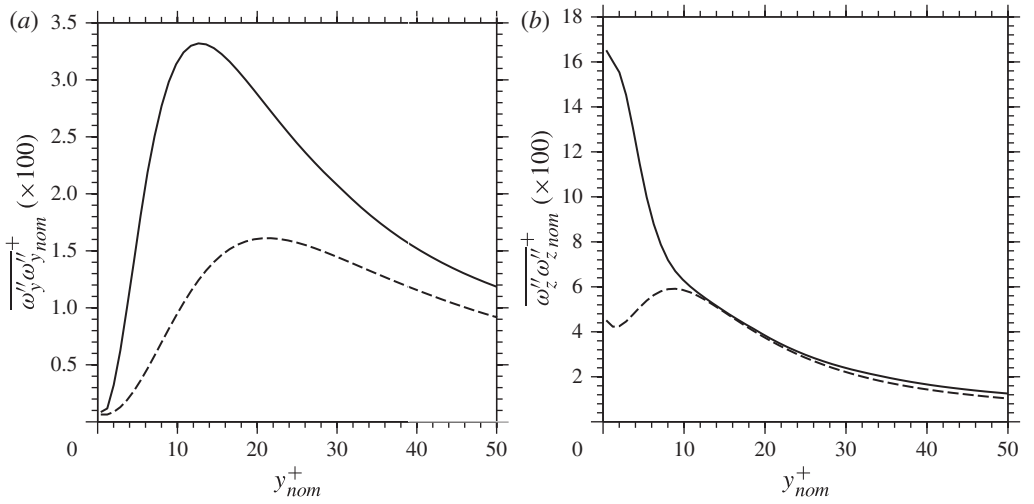

FIGURE 4. Components of the enstrophy in (*a*) the wall-normal direction and (*b*) the spanwise direction, at $T^+ = 100$ (dashed lines), relative to the baseline flow (solid lines).

sublayer, where the Stokes-strain-induced skewness is large and especially disruptive. As observed from the turbulence-energy budget (not included), this reduction is further enhanced by the decrease in viscous diffusion of turbulence towards the wall, and thus in the balancing dissipation, in response to the actuation-induced depression of production in the upper region of the viscous sublayer. The intimate link between dissipation and enstrophy will be pursued further in the discussion of phase-averaged properties in § 3.2.5.

3.2. *Phase-averaged properties*

3.2.1. *Overview*

This section deals with the phase-wise variations of the turbulence properties during the actuation cycle around the low-drag state. With few exceptions, the considerations are restricted to $T^+ = 200$, because it is only at this value that significant periodic fluctuations arise around the low-drag state.

In Touber & Leschziner (2012), an argument is presented that links the phase-wise damping and amplification of the streaks and their orientations to the shear-strain magnitude and the phase-wise rate of change in that strain during the actuation cycle around the location at which the streaks are most vigorous, i.e. $y^+ \approx 12$–15. This argument is revisited, scrutinized and augmented in the following discussion. To this end, phase-wise variations of various phase-averaged turbulence properties, including second moments and their respective production rates, are examined over the actuation period, juxtaposed with phase-wise variations of the skin friction and/or properties of the unsteady strain rate. It will be shown, by reference to properties in the lower regions of the viscous sublayer, that the inter-dependence identified by Touber & Leschziner (2012) is part of a more complex scenario than that was derived previously from observations of interactions in the upper portion of the viscous sublayer. Specifically, localized regions of high velocity skewness in the lower part of the viscous sublayer are identified as promoting the drag-reduction process and as causing a distinctive hysteresis in all turbulence properties within any

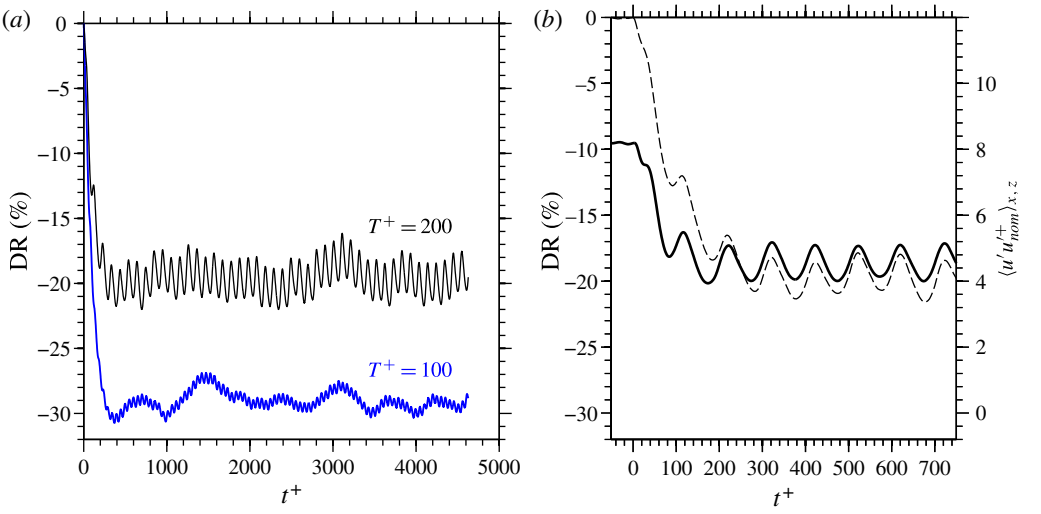

FIGURE 5. (Colour online) Temporal variation of (*a*) the wall-integrated skin-friction reduction, and (*b*) the skin-friction reduction (dashed line) and the x–z-plane-averaged streamwise stress at $y^+ \approx 13.5$ (solid line) at $T^+ = 200$; $\langle \ldots \rangle$ indicates x–z averaging.

one cycle, wherein the drag-reduction and drag-increase phases do not follow the same path. The role of the skewness in promoting drag reduction is examined by reference to its effects on the enstrophy and its components, with particular emphasis placed on the transfer of enstrophy from the wall-normal component to the spanwise component during the drag-reduction phase. It will finally be argued, on the basis of stress budgets and comparisons between enstrophy and turbulence dissipation, that the latter does not play a decisive role in the drag-reduction process, but that this process is driven by the response of the streaks and turbulence production to temporal variations in the Stokes-strain and spatial variations in the velocity skewness.

3.2.2. *Correspondence between transient drag reduction and drag oscillations around the low-drag state*

Prior to this analysis, it is appropriate to address two preliminary questions. First, are the periodic interactions around the low-drag state compatible with those in the transient process in which the drag decays towards its equilibrium low-drag level following the onset of the actuation? Second, are the phase-averaged statistics convergent? The relevance of these questions emerges from figure 5(*a*), which shows the variations of the skin friction following the onset of the actuation over a period corresponding to 46 and 23 actuation cycles for $T^+ = 100$ and 200, respectively. This figure brings out the five features listed below.

(i) At $T^+ = 100$, the skin friction hardly responds to the actuation. Hence, no useful information can be extracted on the drag-reduction mechanisms at the low-drag state.

(ii) The low-drag state is reached within 2–3 actuation cycles, at both actuation periods. In both cases, this state is reached at around $t^+ \approx 300$. The decrease must be associated with the wall-normal penetration, mainly by viscous diffusion, of the Stokes motion across the sublayer. In non-turbulent conditions, it can readily be shown that the time scale required for perturbations to propagate away from

the wall is $t^+ = y^{+2}$. Hence, subject to purely viscous transport, the time taken for the Stokes motion to penetrate to $y^+ = 13$, at which the streaks are most vigorous, is $t^+ = 170$. In reality, turbulence in the upper portion of the viscous layer will reduce this period by around 30 %, as the turbulent shear stress rises cubically with y and surpasses the viscous stress at $y^+ = 11$. However, clearly the drag begins to drop almost immediately after the onset of the actuation. This implies that processes much closer to the wall are influential, and this points to the presence of another mechanism that is different from that arising from the interactions at $y^+ \approx 13$.

(iii) The transient path, especially at $T^+ = 200$, is characterized by oscillatory features that are akin to those observed around the low-drag state.

(iv) The skin-friction fluctuations at $T^+ = 200$ have a peak-to-trough magnitude of about 20 % of the time-mean drag-reduction margin.

(v) Both skin-friction variations feature, as do the distributions for the baseline case, long-time-scale components, and these identify the *footprinting* of large-scale structures (so-called 'super-streaks') residing in the outer flow.

The question of the correspondence between the processes in the transient and the periodic fluctuations around the low-drag state is addressed, in part, in figure 5(*b*). This conveys the relationship between variations in the skin friction and the x–z-averaged streamwise turbulence intensity along the line $y^+ = 13.5$, where the streaks are most pronounced and also very sensitive to the actuation. The figure covers the transient phase as well as a portion that can justifiably be regarded as part of the low-drag state. It shows that reductions/increases in drag and turbulence intensity are closely correlated across the entire temporal range. This provides a first indication that the transient phase is not exceptional, and that a focus on the low-drag state is appropriate, a conclusion strengthened by analogous observations of dissipation and enstrophy variations, presented in the discussion to follow.

Regarding the convergence of phase-averaged statistics, it is observed first, by reference to figure 5(*b*), that the variation in the streamwise stress within any one phase is quite smooth, and that variations from one cycle to another are modest. The former reflects the fact that any point in this distribution arises from averaging over 2 million values, while cycle-to-cycle variations arise from outer large-scale structures. The spatial features of these structures are brought out in figure 6 in which a snapshot of the streamwise-velocity fluctuations in a $\pi h \times 2\pi h$ portion of the $x - z$ plane at $y^+ = 13.5$ is included in three forms: the full field in (*a*), the large-scale structures in (*b*) and the small-scale difference in (*c*). This decomposition was achieved with the Hilbert–Huang transform (Huang *et al.* 1998). The length of the large-scale structures is $O(10^4)$ wall units (of order 10 channel half-heights), corresponding to a convective time scale $t_c^+ \approx 600$ (assuming a convective velocity $U^+ = O(15)$ in the log layer), which is broadly consistent with the long-time-scale fluctuations seen in figure 5(*a*). As an aside, it is remarked that figure 6 illustrates the processes of 'footprinting' by the outer structures on the near-wall flow and of 'modulation' of the small-scale streaks by the large-scale motions, in the sense described by Hutchins *et al.* (2011), Marusic, Mathis & Hutchins (2010). These features are of particular interest in the context of the observed Reynolds-number dependence of the drag-reduction effectiveness, a subject that is outside the scope of the present paper, however.

The significant duration of the large-scale fluctuations, relative to the total simulation period, must mean that the phase-averaged fields cannot be fully converged,

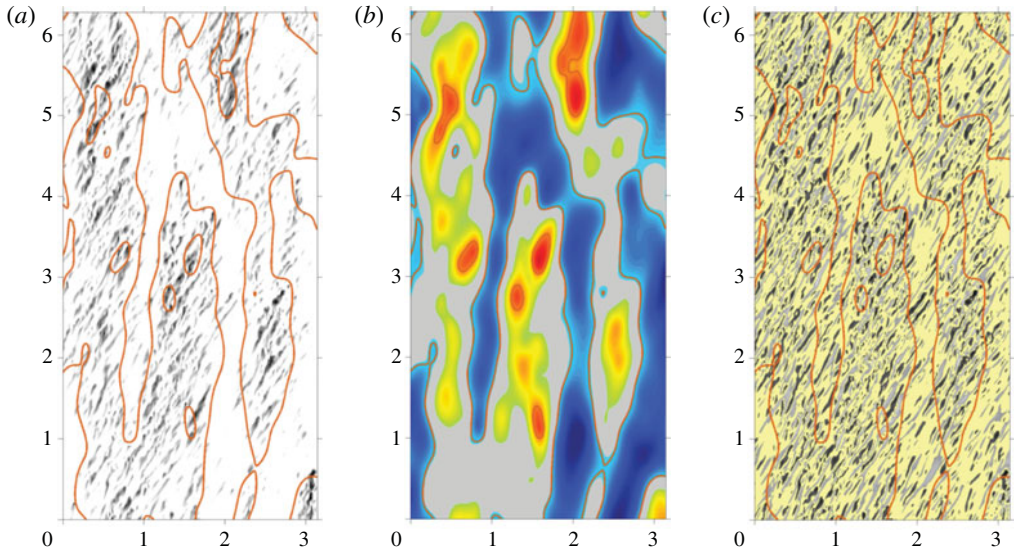

FIGURE 6. Application of the Hilbert–Huang transform to the field of streamwise-velocity fluctuations at $y^+ = 13.5$, at the phase-location of maximum skin friction. (*a*) Raw fluctuation field. (*b*) Large-scale velocity fluctuations (fourth Hilbert–Huang mode), red contours: positive fluctuations; blue contours: negative fluctuations. (*c*) Small-scale velocity fluctuations (first three Hilbert–Huang modes). Small-scale fluctuations are included only above a magnitude of 7 % of the r.m.s. velocity at $y^+ = 13.5$; large-scale velocity fluctuations are included above a magnitude of 9 %. The scales next to domain length and width are multiples of channel half-height.

despite the fair smoothness observed for all properties within any one actuation period. However, the error is small, as illustrated by figure 7 for the skin friction, figure 7(*a*,*c*), and the streamwise normal stress at $y^+ = 13.5$, figure 7(*b*,*d*). The top plots, figure 7(*a*,*b*), show the actual signals, identifying the cycle-to-cycle variations, and also include the large-scale fluctuations derived from the Hilbert–Huang transform (dashed lines). Each of the bottom plots, figure 7(*c*), contains two almost identical lines (solid black and grey), showing the averages of all cycles, one with and the other without the large-scale contributions. The latter plots also include two sets of vertical bars that give a statistical (root-mean-square, r.m.s.) measure of the cycle-to-cycle variation, namely $2(\sum_{cycles}(a - \tilde{a})^2)^{0.5}$, where a is either the skin friction or the normal stress, with the longer bars relating to the actual cycles and the short bars to the cycles from which the large-scale fluctuations have been removed. The fact that the average of the actual cycles and that of the filtered cycles are very close indicates that any errors in the turbulent correlations arising from not removing the large-scale motions are low. In view of the very high processing costs involved in filtering all turbulence data, this filtering has not been performed in the results presented hereafter. The conclusion that the errors are low is strengthened by the fact that tests with averaging over 10 cycles gave fields very close to those with averaging over all cycles in the low-drag range.

3.2.3. *Interactions in the upper part of the viscous sublayer*

The cycle-averaged skin-friction distribution is shown in figure 8, together with the phase-wise variation of the Stokes strain and its phase-wise derivative. The reason

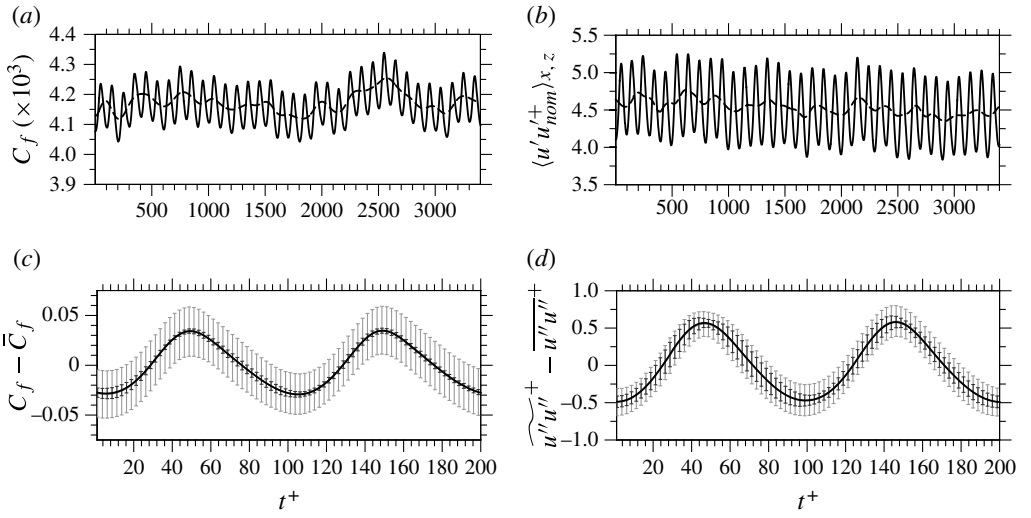

FIGURE 7. Cycle-to-cycle variations due to large-time-scale fluctuations: (*a*) temporal variation of wall-averaged skin friction and its large-time-scale component (dashed line); (*b*) as (*a*), but for *x*–*z*-plane-averaged streamwise Reynolds stress at $y^+ = 13.5$; (*c*) average over all cycles with (black line) and without (grey line) filtering of the large scales, and vertical bars indicating twice the r.m.s. of the cycle-to-cycle differences with (short bars) and without (long bars) filtering of the large scales; (*d*) as (*c*), but for *x*–*z*-plane-averaged streamwise Reynolds stress at $y^+ = 13.5$.

for including the latter is that Touber & Leschziner (2012) link the streak damping and amplification during an actuation phase to the phase-wise rate of change in the strain vector in the upper portion of the viscous sublayer. The horizontal-dashed line in the Stokes-strain plots is at $y^+ = 13.5$, the level around which several of the turbulence quantities reach their maximum values, including the streamwise and spanwise turbulence intensities. Consistent with observations made in Touber & Leschziner (2012), figure 8 shows that the skin friction rises when the Stokes strain in the upper portion of the viscous sublayer is high and 'lingers', while it decreases when the strain is low and changes rapidly with the phase. Thus, the maximum skin friction is attained after a sustained period of high Stokes strain, while the minimum is reached following a sustained period of low and rapidly changing strain. It is emphasized, however, that these interactions are specific to the level at which the streaks are strongest.

Next, figure 9 demonstrates that the streamwise and spanwise stresses, figure 9(*a*,*b*), and their respective production rates, figure 9(*c*,*d*), all reach maxima at $y^+ \approx 13$–15, and that these peaks are well correlated, in phase, with skin-friction maxima, the productions leading the respective stresses by a small phase margin. The peak spanwise stress is substantial, reaching about 50 % of the peak streamwise stress, and this reflects the high rate of Stokes-strain-driven production in the upper portion of the viscous sublayer at the non-optimum actuation period considered. This production is positive almost throughout the phase-space domain, but closer examination reveals it to be marginally negative around the locus at which the Stokes strain vanishes, and hence where it changes most rapidly in phase. Corresponding to the above correlation of maxima, the lowest values in the stresses and their productions, again at $y^+ \approx 13$–15, correlate well with the skin-friction minima.

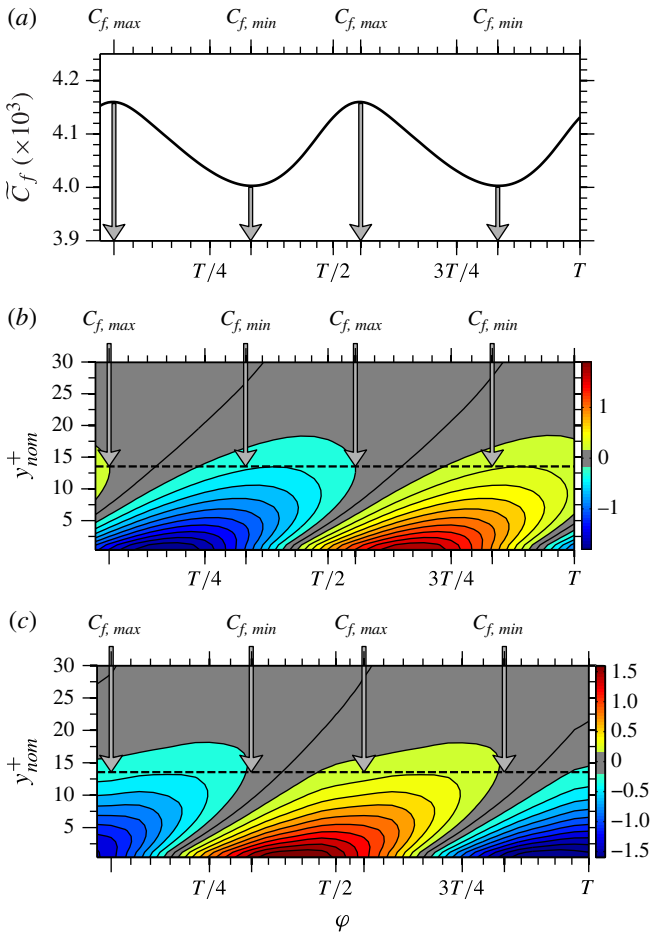

FIGURE 8. Comparison between (*a*) phase-wise cycle-averaged skin-friction fluctuations, (*b*) contours of the Stokes strain ($\partial\widetilde{W}/\partial y$) and (*c*) contours of the phase-wise derivative of the Stokes strain, all at $T^+ = 200$

The behaviour described above accords well with observations by Touber & Leschziner (2012) on the response of the streaks to the Stokes strain at $Re_\tau = 500$. Thus, the streaks are observed to be well-established when the skin friction reaches a maximum, while they are weak, disorganized and ill-defined when the skin friction is at its minimum. Moreover, when the streaks are well-defined, their orientation in the wall-parallel plane is dictated by the magnitude and direction of the total strain in the upper portion of the viscous sublayer. Shortly after the Stokes strain at this position peaks – the lag being around $0.1T^+$ – the streaks are re-established in a direction that is in harmony with the sign of the Stokes strain. Hence, as demonstrated by figure 10(*a*,*c*), the streaks assume two orientations within any one cycle, corresponding to the two lobes of the Stokes strain shown in figure 8.

While the above scenario explains the interactions linking variations in streak strength to the Stokes strain, the explanation for the downward trend in the drag towards a reduced time-averaged level relies on the validity of the streak-amplification time scale as derived from the GOP theory by Blesbois *et al.* (2013). Thus, following

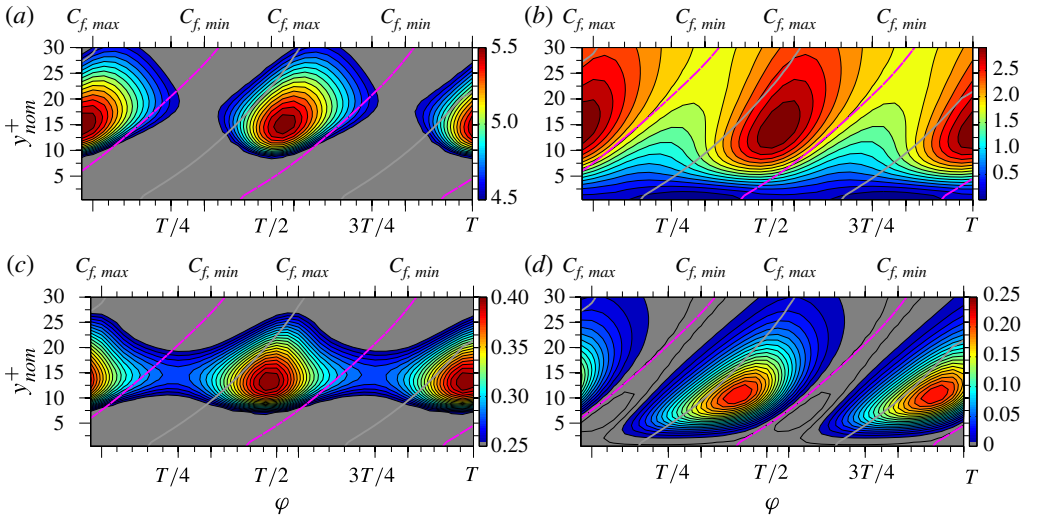

FIGURE 9. Phase-wise variations of (*a*) the streamwise Reynolds stress ($\widetilde{u''u''}$), (*b*) the spanwise Reynolds stress ($\widetilde{w''w''}$), (*c*) the production of the streamwise Reynolds stress ($P_{\widetilde{u''u''}}$) and (*d*) the production of the spanwise Reynolds stress ($P_{\widetilde{w''w''}}$), all at $T^+ = 200$. All quantities are normalized with the nominal friction velocity (grey and magenta curves identify, respectively, the loci of maximum and zero Stokes strain).

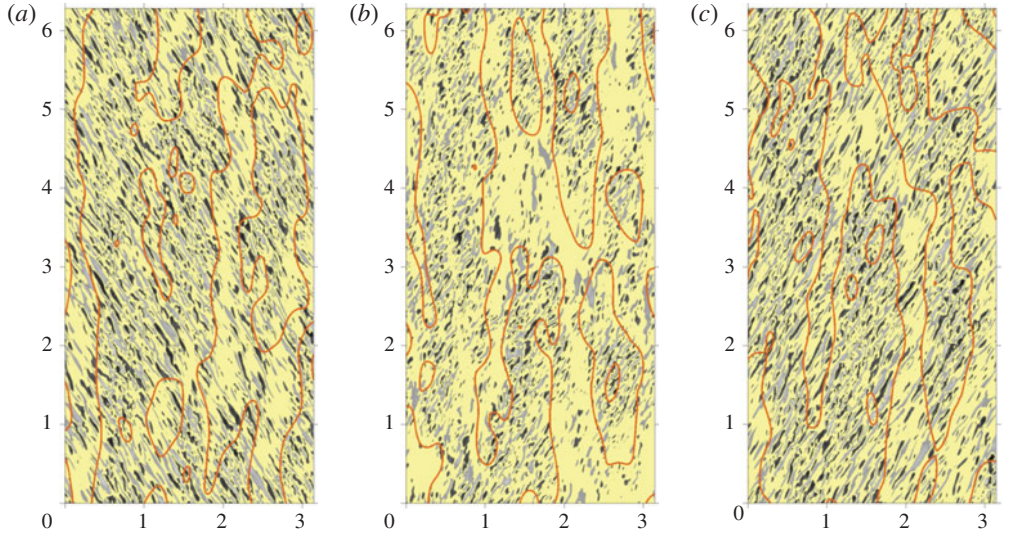

FIGURE 10. Streaky near-wall structure at $y^+ = 13.5$, identified by streamwise-velocity fluctuations, at: (*a*) maximum C_f and negative Stokes strain; (*b*) minimum C_f; (*c*) maximum C_f and positive Stokes strain. Contours identify large-scale motions (fourth Hilbert–Huang mode). For contour details, refer to figure 6.

a reduction phase, the subsequent recovery is constrained by this time scale, which is $t^+ \approx 80$. If the actuation period is too short, the recovery phase is insufficiently long for a complete recovery, and the average drag is thus lowered.

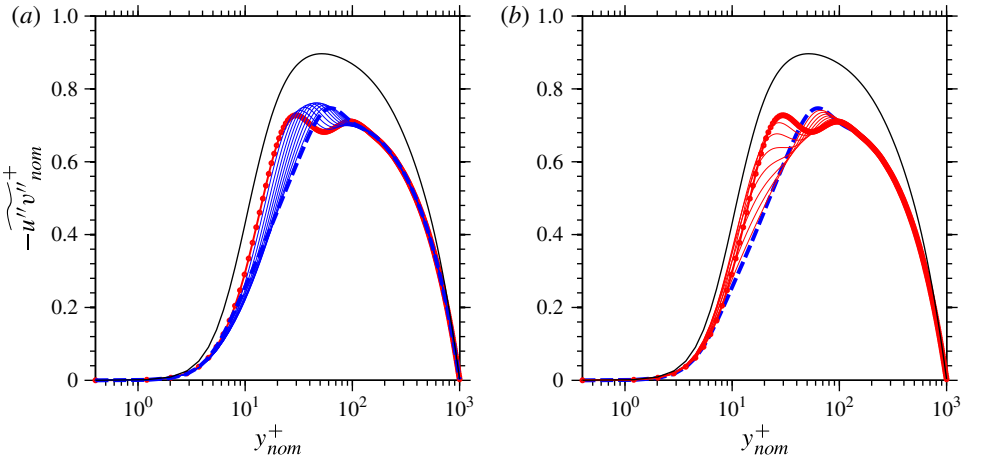

FIGURE 11. (Colour online) Phase-wise variations of profiles of the shear stress during (*a*) the drag-reduction phase and (*b*) the drag-increase phase, at $T^+ = 200$. Thick solid lines with solid circles correspond to the maximum skin-friction phase value; thick dashed lines correspond to minimum skin-friction phase value; thick solid (black) lines correspond to the shear-stress profile obtained in the unactuated flow; thin solid (blue and red online) lines relate to different phases.

3.2.4. *Interactions in the lower part of the viscous sublayer: hysteresis and skewness*

Two features that Touber & Leschziner (2012)'s paradigm cannot explain are, first, the observed reduction in drag that sets in almost immediately after the start of the actuation, figure 5, and second, a striking hysteresis observed in all properties during the action cycle, wherein the drag-reduction phase occurs over a longer part of the cycle than the drag-recovery phase. This hysteresis is clearly visible in the skin-friction variation in figure 8. In quantitative terms, the maximum rate of change in the skin friction during the two phases can be shown to correspond to that of sinusoidal variations with periods $T^+ = 120$ and 80, respectively. Associated with the hysteresis in skin friction are phase-wise asymmetries in all turbulence properties and statistics. This hysteresis can only be explained by a process that is phase-wise asymmetric with respect to the cycle mid-point, and one that favours the drag-reduction phase relative to the drag-recovery phase. In what follows, it is argued that the hysteresis is linked to a phase-wise asymmetric behaviour of the flow skewness – the wall-normal gradient of the velocity-vector direction. While the presence of a hysteresis in flows subjected to spanwise oscillation has been observed before, for example by Skote (2012), it has received little attention so far in terms of its connection to drag-reduction mechanisms. Figures 11 and 12 exemplify the hysteresis in some important turbulence quantities.

First, figure 11 shows the profiles of the phase-averaged shear stress at different phase positions during the actuation cycle. Figure 11(*a*) relates to the period in which the drag (C_f) decreases from its maximum to its minimum, while figure 11(*b*) pertains to the following drag-rise period. During the reduction phase, the shear stress within the viscous sublayer drops progressively and uniformly within $y^+ \approx 30$, with the maximum stress shifting outwards by about 30 wall units. In the drag-rise phase, the shear stress increases again, but it is remarkable that this increase does not follow the same path as the preceding decrease, i.e. the cyclic process is hysteretic. In

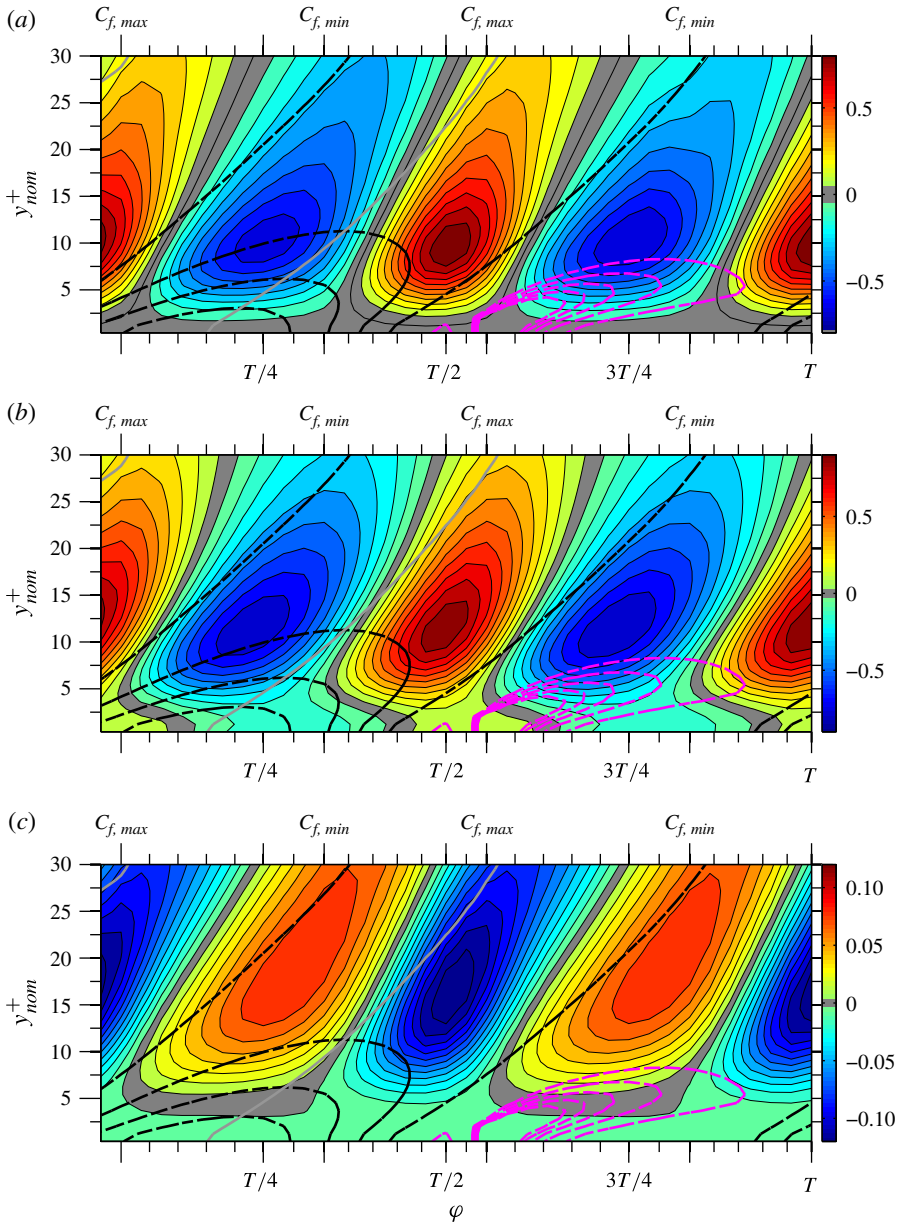

FIGURE 12. Phase-wise variations of fluctuations in (*a*) the streamwise stress ($\widetilde{u''u''}^+ - \overline{u''u''}^+$), (*b*) the spanwise stress ($\widetilde{w''w''}^+ - \overline{w''w''}^+$), and (*c*) the shear-stress ($\widetilde{u''v''}^+ - \overline{u''v''}^+$). Dashed contours represent loci of 75 %, 50 %, 25 % and 0 % of the maximum absolute value of the Stokes strain.

particular, the rise in the shear stress occurs preferentially in the near-wall layer, with an increase close to the wall propagating outwards across the sublayer, the maximum at around $y^+ \approx 25$ being re-established much more quickly than it had been eroded in the preceding drag-decrease phase.

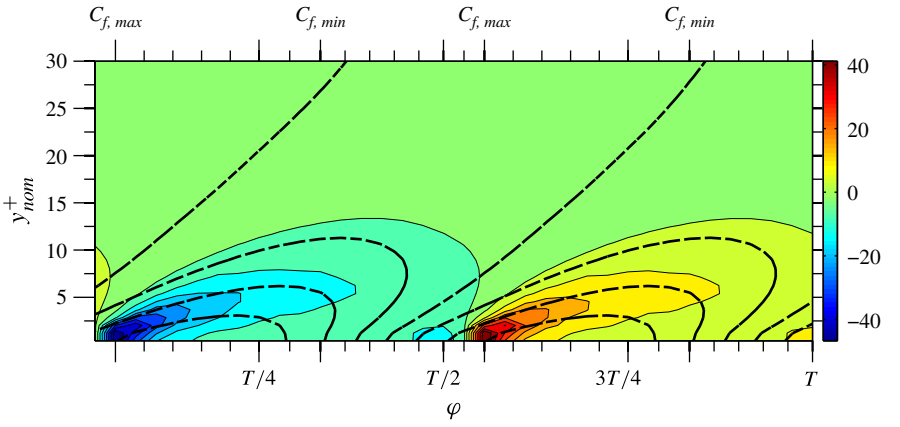

FIGURE 13. Skewness map (wall-normal derivative of velocity angle). Dashed contours represent loci of 75 %, 50 %, 25 % and 0 % of the maximum absolute value of the Stokes strain.

The hysteresis is brought out well in figure 12, which shows phase-wise contour plots of fluctuations in the streamwise normal stress, $(\widetilde{u''u''}^+ - \overline{u''u''}^+)$, the spanwise normal stress, $(\widetilde{w''w''}^+ - \overline{w''w''}^+)$ and the stress $(\widetilde{u''v''}^+ - \overline{u''v''}^+)$. The dashed black contour lines indicate, respectively, 75 %, 50 %, 25 % and 0 % of the maximum Stokes-strain magnitude. The relevance of the magenta contours will be explained in the discussion to follow. All plots (and those for other stresses and their production rates that are not included) show that the decrease in the magnitude of the stresses progresses over a longer portion of the period than the increase (note that red-coloured contours always indicate positive perturbations, thus corresponding to a reduction in the magnitude of the shear stress).

The question that is addressed next is what causes the hysteresis. It is observed first that the causal relationship between the Stokes strain and the stresses at $y^+ \approx 13$–15 (figure 8) does not hold close to the wall. Specifically, as the wall is approached, the phase-lag between the region of lingering, high Stokes strain and the region of high turbulent-stress levels is increasing, to the extent that the region of high Stokes strain progressively coincides with regions of low turbulent stresses. One explanation might be that the increasing lag reflects an increasing time scale over which turbulence is amplified. However, this neither accords with the accepted view that the time scale of turbulence events in the viscous sublayer is some weighted combination of the eddy-turnover time scale k/ε (k is the turbulence energy and ε its dissipation rate) and the Kolmogorov time scale $(\nu/\varepsilon)^{1/2}$, nor with statements derived from the GOP theory. The above two limiting time scales suggest that the weighted combination will reduce towards the wall, because k decreases in proportion to y^2, and will reach some finite plateau governed by the finite wall value of the dissipation. The GOP predicts, likewise, that the amplification time scale reduces towards the wall, although by a modest amount, based on computations for the range $y^+ = 6$–16.

Another possible source is a property of the Stokes strain that is likely to disrupt the streak-formation process and has a distinct phase-wise asymmetric character. Such a property is the flow skewness, $\partial\theta/\partial y$, where θ is the velocity-vector orientation. Contours of the skewness are shown in figure 13, relative to Stokes-strain contours, and these are also included, in the form of dashed magenta lines, in figure 12. The

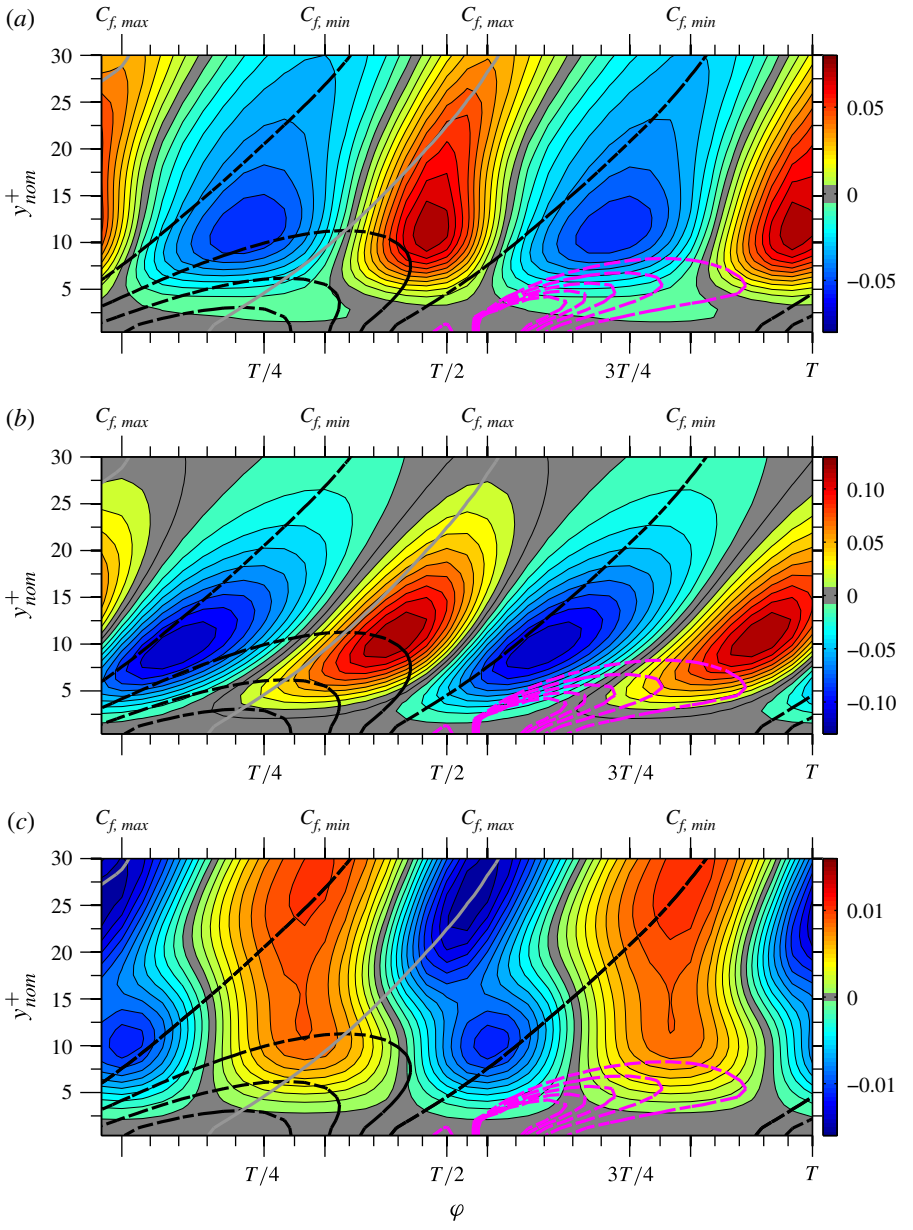

FIGURE 14. Phase-wise variations in the production fluctuations in (*a*) the streamwise stress ($P_{\widetilde{u''u''}^+} - P_{\overline{u''u''}^+}$), (*b*) the spanwise stress ($P_{\widetilde{w''w''}^+} - P_{\overline{w''w''}^+}$), and (*c*) the shear stress ($P_{\widetilde{u''v''}^+} - P_{\overline{u''v''}^+}$). The grey line is the locus of maximum Stokes strain. The dashed magenta contours indicate skewness levels.

skewness is observed to be very high within a tongue that originates at the location $C_{f,max}$ and traverses the lower portion of the viscous sublayer in which the stresses are depressed. Importantly, the high-skewness region only covers the phase portion during which the drag decreases. Moreover, figure 14 shows that high levels of skewness,

again identified by the dashed magenta contours, coincide with near-wall regions in which the production of the streamwise and shear stresses are depressed, despite the high level of the Stokes strain. The exception is the production of the spanwise stress $P_{\widetilde{w''w''}+}$ which is linearly dependent on the Stokes strain and thus directly driven by it. While this is not claimed to be a proof of the origin of the hysteresis and the near-wall suppression of turbulence, the distinct asymmetry of this property and its coincidence with areas of turbulence suppression is striking, and provides credible evidence that skewness is the source of the hysteresis. It causes a prolongation of the drag-reduction phase, relative to the phase of drag increase, and shortens the period over which the streaks are allowed to re-establish against the GOP-predicted streak-amplification time scale $t^+ \approx 80$. Thus, at $T^+ = 200$, the streak-regeneration time interval is $t^+ \approx 40$, while at $T^+ = 100$, this value decreases to about 20, effectively preventing the re-generation of the streaks and resulting in the insensitivity to the oscillatory actuation around the low-drag state (see figure 5*a*). The fact that the skewness depresses the turbulent level very close to the wall also suggests that it plays an important role in the initial decay of the drag immediately after the onset of the actuation. In fact, at this early stage, skewness is exceptionally high, as the Stokes layer is very thin, so that its effect is likely to be more pronounced than the mechanism in the upper portion of the viscous sublayer, when the Stokes motion has spread across the layer after approximately one half of the actuation period. The fact that the turbulence intensity in the upper portion of the viscous sublayer also begins to decrease very shortly after the actuation starts – as is seen from figure 5 – reflect a coupling, via pressure fluctuations, between the near-wall reduction in ejections very close to the wall and the wall-normal fluctuations at higher elevations. Results obtained (but not included herein) for the time-evolution of the budget $\langle v''v'' \rangle_{x,z}$ in the transient period have revealed a rapid decrease in the pressure–velocity interaction across the near-wall layer very shortly after the start of the actuation, within $t^+ = 10$–20. As this interaction is the principal source driving $\langle v''v'' \rangle_{x,z}$, its decrease leads to a reduction in that stress and consequently a reduction in the shear stress, the production of which is proportional to $\langle v''v'' \rangle_{x,z}$.

3.2.5. *Dissipation and enstrophy*

An important issue to address, in view of previous studies (e.g. Ricco *et al.* 2012), is whether the dissipation and enstrophy play critical roles in driving the drag-reduction process. This is considered next, by reference to stress budgets and enstrophy plots.

First, figures 15 and 16 show phase-wise variations of the budgets for the streamwise and the shear stress components, respectively. In the present case of channel flow, the budgets can be expressed by the following equations, which also define the terms plotted in the figures:

$$\frac{\partial \widetilde{u''u''}}{\partial t} = \underbrace{-\frac{\partial \widetilde{u''u''v''}}{\partial y}}_{\text{tdiff}} \underbrace{-2\widetilde{u''\frac{\partial p''}{\partial x}}}_{\text{pvel}} \underbrace{-2\widetilde{u''v''}\frac{\partial \widetilde{U}}{\partial y}}_{\text{prod}} \underbrace{-\frac{2}{Re}\sum_{i=1}^{3}\widetilde{\left(\frac{\partial u''}{\partial x_i}\right)^2}}_{\text{diss}} + \underbrace{\frac{1}{Re}\frac{\partial^2 \widetilde{u''u''}}{\partial y^2}}_{\text{vdiff}}, \tag{3.3}$$

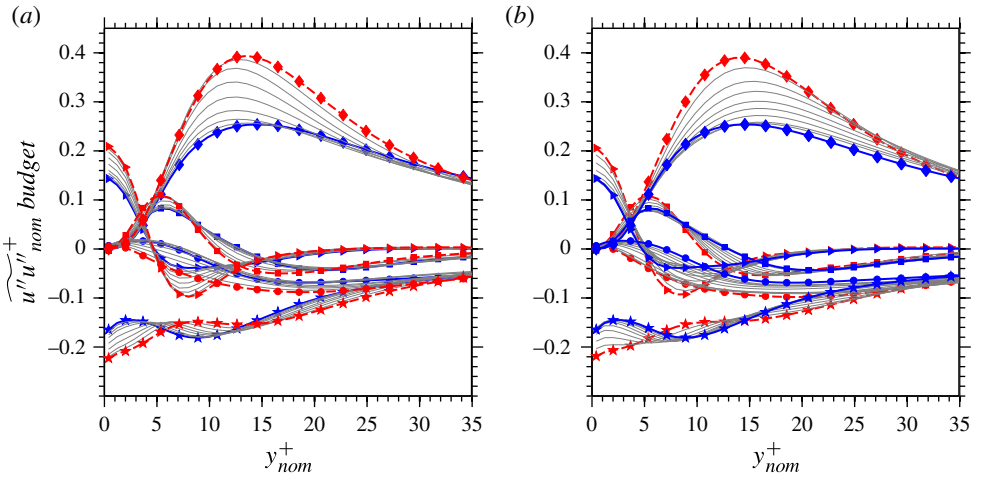

FIGURE 15. (Colour online) Phase-wise fluctuations of the budget contributions for the streamwise normal stress during (*a*) the drag-increase phase and (*b*) the drag-decrease phase. Thick dashed lines with symbols correspond to the maximum skin-friction phase value; thick solid lines with symbols correspond to minimum skin-friction phase value; thin lines identify intermediate phases; budget terms are defined by: ♦ production, ■ turbulent diffusion, ▲ viscous diffusion, ● pressure–velocity interaction, ★ dissipation.

$$\frac{\partial \widetilde{u''v''}}{\partial t} = \underbrace{-\frac{\partial \widetilde{u''v''v''}}{\partial y}}_{\text{tdiff}} \underbrace{\widetilde{-u''\frac{\partial p''}{\partial y}} - \widetilde{v''\frac{\partial p''}{\partial x}}}_{\text{pvel}} \underbrace{-2\widetilde{v''v''}\frac{\partial \widetilde{U}}{\partial y}}_{\text{prod}}$$
$$\underbrace{-\frac{2}{Re}\sum_{i=1}^{3}\widetilde{\left(\frac{\partial u''v''}{\partial x_i}\right)^2}}_{\text{diss}} + \underbrace{\frac{1}{Re}\frac{\partial^2 \widetilde{u''v''}}{\partial y^2}}_{\text{vdiff}}. \tag{3.4}$$

For each stress, two sets of plots are presented: plot (*a*) in each set relates to the drag-rise phase, while plot (*b*) relates to the drag-decrease phase, the phase values at which C_f reaches its maximum and minimum being indicated by the thicker solid lines with symbols. The imbalance in the budgets presented in figures 15 and 16 is shown in figure 17. The three curves in each plot relate, respectively, to the minimum- and maximum-C_f phase positions and to the phase-average. The last should be zero, and the modest imbalance – a maximum of 0.02 in the case of the streamwise stress and much lower in the case of the shear stress – is indicative of the error margin arising from the complex process of determining the budget for the stochastic correlations. However, the phase-wise departure of the imbalance from the phase average was found to agree well with distributions obtained from the phase-wise gradient of the stresses, i.e. the left-hand sides of (3.3) and (3.4). Clearly, this unsteady contribution is a small difference between large contributions, and its determination from the imbalance – the right-hand side of (3.3) and (3.4) – is difficult and prone to some error. The most important point to highlight in the $\widetilde{u''u''}^{+}$ budget is that the substantial fluctuations in production over most of the near-wall layer, reflecting variations in the streak strength and driving the normal-stress fluctuations,

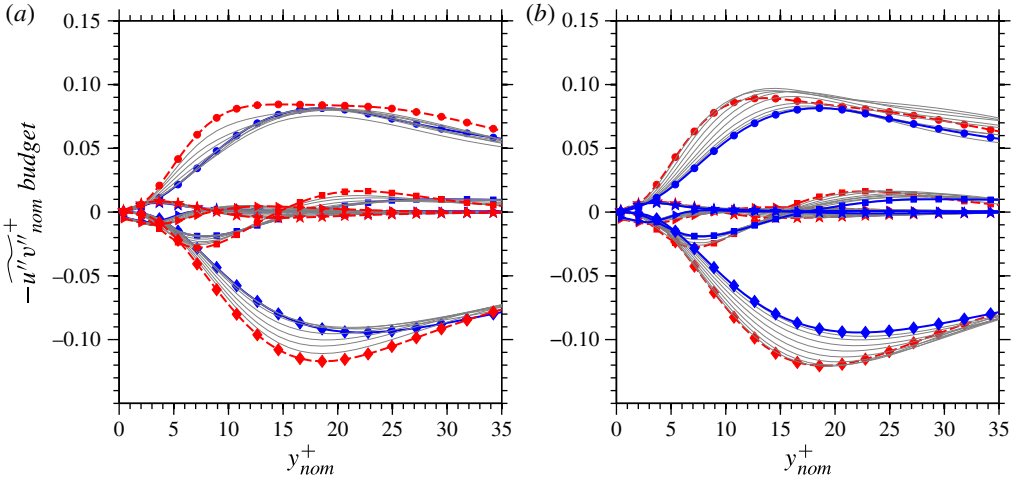

FIGURE 16. (Colour online) Phase-wise fluctuations of the budget contributions for the shear stress during (*a*) the drag-increase phase and (*b*) the drag-decrease phase. Lines and symbols have the same meaning as in figure 15.

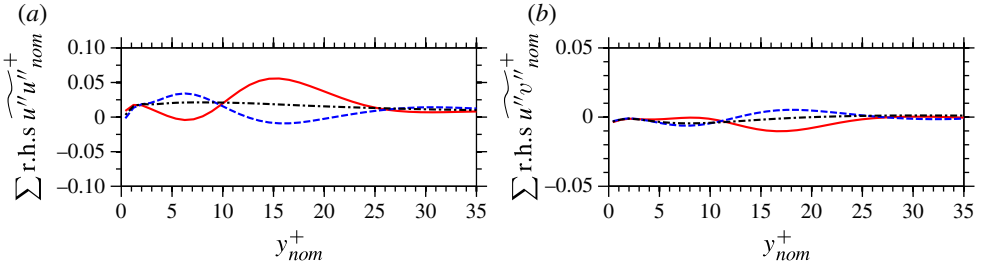

FIGURE 17. (Colour online) Imbalance in the budgets (sum of the right-hand sides of (3.3) and (3.4)) for (*a*) the streamwise stress and (*b*) the shear stress. Solid line corresponds to the maximum C_f phase; dashed line corresponds to the minimum C_f phase; chain line relates to the time average.

are balanced mainly by corresponding fluctuations in diffusion and pressure–velocity interaction. In contrast, variations in the dissipation level are fairly small. Moreover, during the drag-reduction phase, the dissipation decreases over almost the entire wall-normal extent, with the reverse occurring during the drag-increase phase. Very close to the wall the behaviour is different. Here, dissipation has to balance viscous diffusion. Both increase during the drag-increase phase and decrease during the drag-decrease phase. However, near-wall diffusion rises and falls, because the high production away from the wall rises and falls, and this leads to diffusion of energy away from the production maximum to either side of this maximum. Hence, at the wall, variations in dissipation are driven by (and are the consequence of) variations in production. A qualitatively similar behaviour is observed in the case of the shear-stress budget, although here, the significant fluctuations in production are balanced by corresponding fluctuations in the pressure–velocity interaction, while the dissipation is almost insignificant, reflecting the near-isotropy of the small-scale dissipative motions. Hence, any influence exercised by the dissipation of the shear

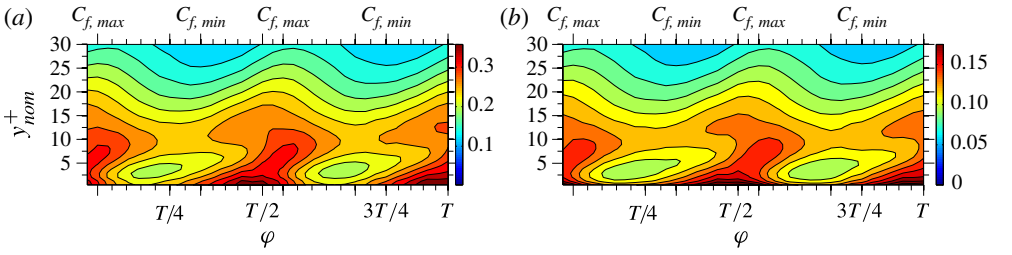

FIGURE 18. Phase variation of (*a*) turbulence-energy dissipation (ε_{ii}), (*b*) enstrophy ($\widetilde{\omega_i''\omega_i''}$).

stress, and thus drag-reduction process, cannot be direct, but has to proceed via the linkage between turbulence energy and the shear stress.

These observations, especially the harmony between the trends of drag and dissipation, and the modest phase-wise changes in the dissipation relative to other processes in the budget, are at odds with the mechanism proposed by Ricco *et al.* (2012), which is based on the argument that the enstrophy is enhanced by the Stokes motion, and thus the increase in enstrophy and dissipation are held responsible for the drag reduction. This contradiction will be reinforced by results for the enstrophy discussed below.

The relationship between dissipation and enstrophy is examined by reference to phase-averaged results for the enstrophy and its components. First, figure 18 compares phase-wise variations of the enstrophy and of the dissipation of turbulence energy. Entirely in accord with expectations, the two are found to be closely correlated. Importantly, both decrease during the phase in which the drag decreases, and rise when the drag increases.

At this point, it is opportune to return to the correspondence between the transient phase of the drag-reduction process and the oscillations around the low-drag state, first considered in figure 5. Figure 19 compares contours of dissipation and enstrophy, in a manner analogous to that in figure 18. Also included in the figure is a comparison between the y-wise-integrated dissipation rate and the skin friction during the transient process. The conclusion is, here again, that the transient phase shows no exceptional features, and that the relationship between dissipation and enstrophy does not change, both declining during phases of drag decrease and rising with increasing drag within any one cycle. Moreover, the transient phase of the flow at $T^+ = 100$ (not included) shows exactly the same correspondence. The overall level of dissipation and enstrophy decrease during the initial 2–3 actuation cycles, but this decrease is modest, and the fluctuations around the low-drag state give an appearance that is very similar to that in the transient phase. One unusual feature in figure 19 is a thin tongue of elevated dissipation and enstrophy immediately after the onset of the actuation. This is due, to a minor glitch in the imposition of the plate motion, with the plate velocity having a small finite value at the time the actuation starts, thus causing a temporal discontinuity in the Stokes strain at the wall. The time interval over which this discontinuity affects the flow is $t^+ \approx 10$. Reference to figure 5(*b*) shows that this is a very small portion of the transient period, during which the skin friction hardly changes. The fact that the skin friction begins to drop within this interval reflects the extremely high near-wall skewness associated with the discontinuity. Thus, the increase in dissipation in this interval has no bearing on the drag-reduction scenario. Over the entire remaining part

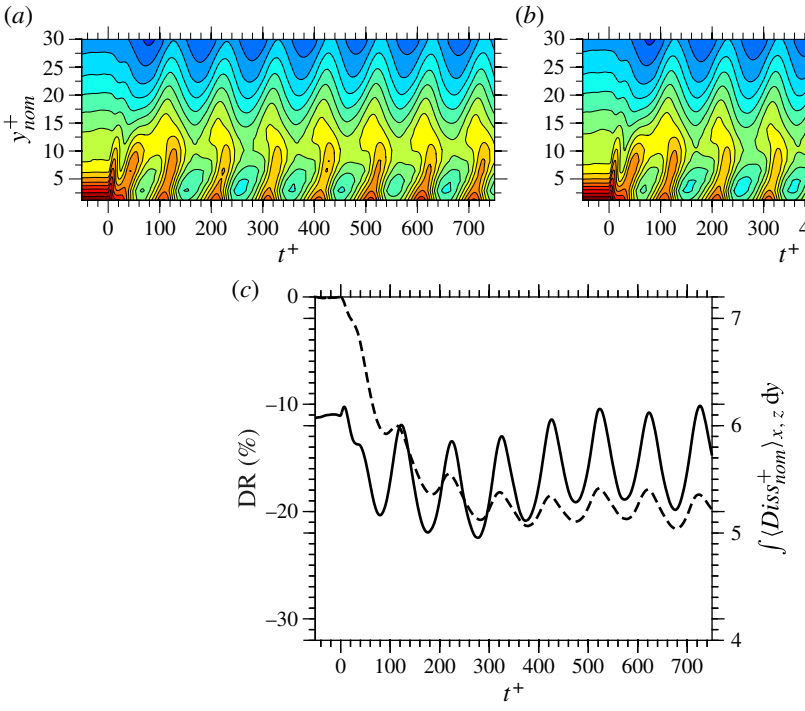

FIGURE 19. Temporal variation of (*a*) dissipation, (*b*) enstrophy during the transient phase, at $T^+ = 200$, and (*c*) skin friction (dashed line) and y-wise-integrated dissipation rate (solid line).

of the transient period, and thereafter, drag reduction is consistently associated with a decrease in dissipation.

3.2.6. *Enstrophy components: interactions with strain and skewness*

Figure 20 shows phase-wise profiles of the enstrophy component, $\widetilde{\omega_y'' \omega_y''}$ (any reference to 'component' should be understood to relate to one of the three constituents that contribute to the scalar enstrophy). This component is being given preference here, because it reflects the significant phase-dependent variations in streak strength and structure during the actuation cycle, although the increase in spanwise velocity fluctuations, due to Stokes-strain-induced production, also contributes, albeit modestly, to the observed phase sensitivity. The results for $T^+ = 100$ are included here to convey the fact that the wall-normal enstrophy component for this value varies only weakly with phase, while its time-averaged value is drastically lower than the corresponding level in the baseline case (see figure 4). This also applies to other enstrophy components not included herein. For example, the spanwise enstrophy component reduced by around 50–75 % of its value in the baseline case within $y^+ \approx 5$, reflecting the reduction in the near-wall dissipation rate. Consistent with properties already presented, the enstrophy also shows a distinctive hysteresis. Starting from the lowest variation, corresponding to the skin-friction trough in figure 8, the enstrophy increases at the fastest rate in the layer $y^+ \approx 6$–15, with the maximum moving upwards in the layer $y^+ \approx 10$–13. In contrast, the decrease is more uniform across the viscous sublayer, with the maximum shifting outwards in the range $y^+ \approx 13$–20.

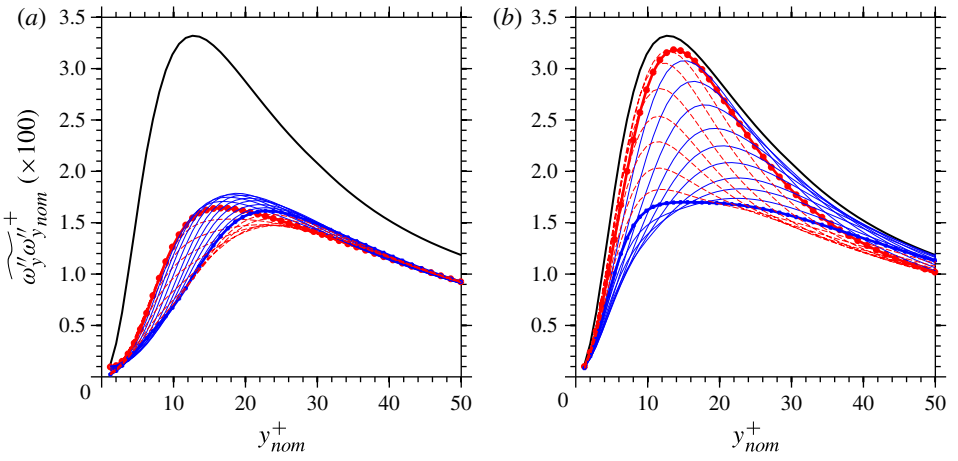

FIGURE 20. (Colour online) Phase-wise variations of the wall-normal component of the enstrophy at (*a*) $T^+ = 100$ and (*b*) at $T^+ = 200$ upper solid (red) lines with symbols correspond to the maximum skin-friction phase value; lower solid (blue) lines with symbols correspond to minimum skin-friction phase value; solid (black) lines without symbols relate to the unactuated flow; thin lines identify intermediate phases.

This behaviour is consistent with the inclination of the $\widetilde{u''u''}^+$ contours in figure 12, the rise following a region of high, lingering Stokes strain, and the fall driven by a concurrence of a rapidly changing Stokes strain in the upper part of the viscous sublayer and high near-wall skewness.

Phase-space contour maps for three components of the enstrophy and their respective productions, all at $T^+ = 200$, are shown in figure 21. To support the discussion to follow, the equation for the enstrophy and simplified forms of the equations for its three components are given below. The simplification amounts to the insertion of the streamwise and Stokes strains into the components of the rotation vector Ω_i and the lumping of terms not including the mean-strain into the additive fragments T_{xx}, T_{yy} and T_{zz}. Thus, the enstrophy equation is governed by:

$$\begin{aligned}\frac{\partial\widetilde{\omega_i''\omega_i''}}{\partial t} &= -\widetilde{u_j''\omega_i''}\frac{\partial\widetilde{\Omega_i}}{\partial x_j} + \widetilde{\omega_i''\omega_j''}\frac{\partial\widetilde{U}_i}{\partial x_j} + \widetilde{\omega_i''\frac{\partial u_i''}{\partial x_j}}\widetilde{\Omega_j} \\ &\quad + \widetilde{\omega_i''\omega_j''}\frac{\partial u_i''}{\partial x_j} - \frac{1}{2}\frac{\partial(\widetilde{u_j\omega_i''\omega_i''})}{\partial x_j} + \frac{\nu}{2}\frac{\partial^2\widetilde{\omega_i''\omega_i''}}{\partial x_j\partial x_j} - \nu\widetilde{\frac{\partial\omega_i''}{\partial x_j}\frac{\partial\omega_i''}{\partial x_j}},\end{aligned} \tag{3.5}$$

with $\widetilde{\Omega_i} = [\partial\widetilde{W}/\partial y,\ 0,\ -\partial\widetilde{U}/\partial y]$. The equations for the enstrophy components arise as: *x*-component:

$$\begin{aligned}\frac{\partial\widetilde{\omega_x''\omega_x''}}{\partial t} &= -\widetilde{v''\omega_x''}\frac{\partial^2\widetilde{W}}{\partial y^2} + \widetilde{\omega_x''\omega_y''}\frac{\partial\widetilde{U}}{\partial y} + \widetilde{\omega_x''\frac{\partial u''}{\partial x}}\frac{\partial\widetilde{W}}{\partial y} - \widetilde{\omega_x''\frac{\partial u}{\partial z}}\frac{\partial\widetilde{U}}{\partial y} + T_{xx} \\ &= -\widetilde{\omega_x''\frac{\partial v''\frac{\partial\widetilde{W}}{\partial y}}{\partial y}} - \widetilde{\omega_x''\frac{\partial w}{\partial z}}\frac{\partial\widetilde{W}}{\partial y} - \widetilde{\omega_x''\frac{\partial w}{\partial x}}\frac{\partial\widetilde{U}}{\partial y} + T_{xx},\end{aligned} \tag{3.6}$$

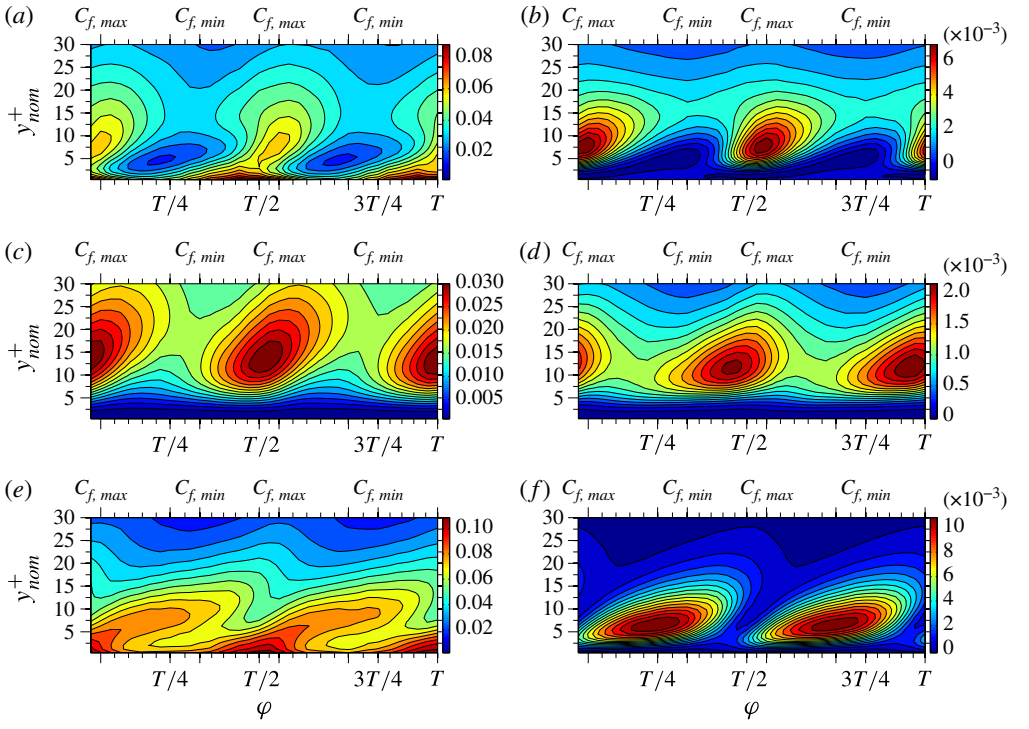

FIGURE 21. Phase variations of the enstrophy components (left-hand column) and their production rates (right-hand column): (*a,b*) *x*-component; (*c,d*) *y*-component; (*e,f*) *z*-component.

y-component:

$$\frac{\partial\widetilde{\omega_y''\omega_y''}}{\partial t} = \widetilde{\omega_y''\frac{\partial v''}{\partial x}}\frac{\partial\widetilde{W}}{\partial y} - \widetilde{\omega_y''\frac{\partial v''}{\partial z}}\frac{\partial\widetilde{U}}{\partial y} + T_{yy}, \tag{3.7}$$

z-component:

$$\begin{aligned}\frac{\partial\widetilde{\omega_z''\omega_z''}}{\partial t} &= \widetilde{v''\omega_z''}\frac{\partial^2\widetilde{U}}{\partial y^2} + \widetilde{\omega_z''\omega_y''}\frac{\partial\widetilde{W}}{\partial y} + \widetilde{\omega_z''\frac{\partial w''}{\partial x}}\frac{\partial\widetilde{W}}{\partial y} - \widetilde{\omega_z''\frac{\partial w''}{\partial z}}\frac{\partial\widetilde{U}}{\partial y} + T_{zz}\\ &= \widetilde{\omega_z''\frac{\partial v''\frac{\partial\widetilde{U}}{\partial y}}{\partial y}} + \widetilde{\omega_z''\frac{\partial u''}{\partial x}}\frac{\partial\widetilde{U}}{\partial y} + \widetilde{\omega_z''\frac{\partial u''}{\partial z}}\frac{\partial\widetilde{W}}{\partial y} + T_{zz}.\end{aligned} \tag{3.8}$$

Phase-averaged budgets (not included), representing (3.6)–(3.8) and featuring most contributions explicitly, show that the major contributions outside the immediate near-wall region, $y^+ > 5$, are mean-strain production and viscous destruction. Hence, production fluctuations are primarily responsible for fluctuations in the enstrophy components.

A first observation derived from figure 21 is that the enstrophy-production rates are well correlated with the respective enstrophy components themselves. Exceptions to this correspondence relate to thin areas very close to the wall in which the link between enstrophy and the high near-wall dissipation governs the former. Second,

the streamwise component drops during the drag-reduction phase, while it rises when the drag and streak strength increase. This accords with expectations, as the phases of low streamwise enstrophy go hand-in-hand with low wall-normal (and spanwise) motions, and hence low wall-normal mixing of streamwise momentum. Third, consistent with low/high streamwise enstrophy are corresponding low/high wall-normal enstrophy levels of $\widetilde{\omega_y''\omega_y''}$. As noted earlier, this component is indicative of the decay and regeneration of the streaks during the actuation period. The fact that this component is relatively low (though fluctuating strongly) is due to the substantial spanwise distances, of order 100 wall units, separating the streak. Here too, the rise and fall of both production and enstrophy are well correlated. Finally, the spanwise component features, unexpectedly at first sight, a rise in the production rate in the region in which the other components show a decrease. In order to gain insight into the origins of this 'anomalous result', it is necessary to examine individual terms in (3.7) and (3.8) by reference to the strain and skewness map given in figure 13. The gradient, $\partial\theta/\partial y$, can be expected to play an important role in the enstrophy equations, because it represents the degree of tilting of vortices by the combined action of the streamwise and Stokes strain. To identify the origin of the unexpected spanwise enstrophy generation, the strain-related production terms are re-written as follows:

$$\begin{aligned}
&\widetilde{\omega_y''\frac{\partial v''}{\partial x}}\frac{\partial \widetilde{W}}{\partial y}-\widetilde{\omega_y''\frac{\partial v''}{\partial z}}\frac{\partial \widetilde{U}}{\partial y}\\
&\quad=\widetilde{\omega_y''\frac{\partial v''}{\partial x}}\sin\theta\frac{\partial \widetilde{U_n}}{\partial y}+\widetilde{\omega_y''\frac{\partial v''}{\partial x}}\widetilde{U_n}\cos\theta\frac{\partial\theta}{\partial y}\\
&\quad\underbrace{-\widetilde{\omega_y''\frac{\partial v''}{\partial z}}\cos\theta\frac{\partial \widetilde{U_n}}{\partial y}}_{\text{figure 22}(a)}+\widetilde{\omega_y''\frac{\partial v''}{\partial z}}\widetilde{U_n}\sin\theta\frac{\partial\theta}{\partial y},
\end{aligned}\tag{3.9}$$

$$\begin{aligned}
&\widetilde{\omega_z''\frac{\partial u''}{\partial z}}\frac{\partial \widetilde{W}}{\partial y}+\widetilde{\omega_z''\frac{\partial u''}{\partial x}}\frac{\partial \widetilde{U}}{\partial y}\\
&\quad=\widetilde{\omega_z''\frac{\partial u''}{\partial z}}\sin\theta\frac{\partial \widetilde{U_n}}{\partial y}+\underbrace{\widetilde{\omega_z''\frac{\partial u''}{\partial z}}\widetilde{U_n}\cos\theta\frac{\partial\theta}{\partial y}}_{\text{figure 22}(b)}\\
&\quad+\widetilde{\omega_z''\frac{\partial u''}{\partial x}}\cos\theta\frac{\partial \widetilde{U_n}}{\partial y}-\widetilde{\omega_z''\frac{\partial u''}{\partial x}}\widetilde{U_n}\sin\theta\frac{\partial\theta}{\partial y}.
\end{aligned}\tag{3.10}$$

The terms proportional to the strain magnitude, $\partial\widetilde{U_n}/\partial y$, may be interpreted as vortex-stretching terms, while the skewness $\partial\theta/\partial y$ dictates the vortex-tilting process. An examination of all fragments in (3.9) and (3.10), not detailed herein, shows that the dominant terms are the third one in (3.9) and the second one in (3.10). Only these two fragments are given in figure 22. Some other terms make non-negligible contributions too, but the present discussion is intended to focus only on the principal processes. Figure 22(*a*) shows that maxima occur at $y^+\approx 15$ at the phase-wise locations at which C_f peaks; this is in agreement with the total production of $\widetilde{\omega_y''\omega_y''}$, which is dominated by the fragment under consideration. These maxima reflect production by streamwise strain in the virtual absence of skewness. Near the wall, on the other hand, there are

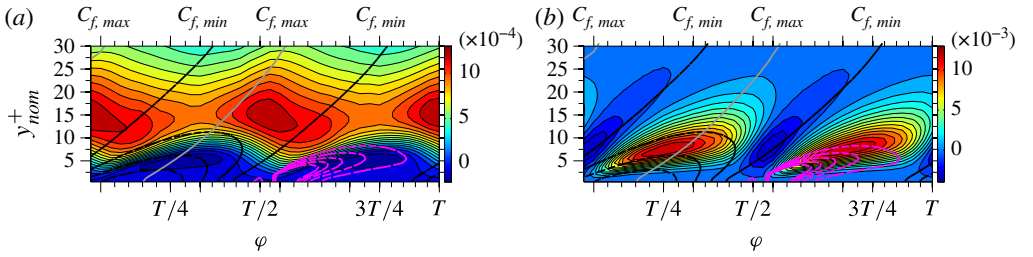

FIGURE 22. Dominant terms in the equations for the y- and z-components of the enstrophy: (a) third term in (3.9); (b) second term in (3.10).

regions of very low production, and these are also regions of very high skewness. Here, $\widetilde{\omega_y''\omega_y''}$ decreases, and this is linked to the high levels of $\widetilde{\omega_z''\omega_z''}$ production, seen in figure 22(b), and due to the high level of skewness. In these regions, the Stokes strain is very high, and the tilting associated with this strain transfers enstrophy from the wall-normal component to the spanwise component, which is then amplified by the high skewness. Analogous interactions also occur between $\widetilde{\omega_x''\omega_x''}$ and $\widetilde{\omega_z''\omega_z''}$, but these are not pursued herein. The transfer and amplification process identified above gives rise to $\widetilde{\omega_z''\omega_z''}$ production peaks that coincide with the locations $C_{f,min}$ rather that $C_{f,max}$, which then leads to the field shown in figure 21(f).

4. Summary and conclusions

The main thrust of this study was directed towards a clarification of the drag-reduction mechanisms, and thus entailed an examination of the phase-averaged fields of stochastic stresses, their budgets and enstrophy components at $T^+ = 200$. Skin-friction fluctuations were found to correlate closely with the streamwise turbulence intensity and its production at the wall-normal region in which the streaks have the highest intensity. This correspondence also applies to the transient phase, ahead of the low-drag state.

The present results display features that comply with the scenario described by Touber & Leschziner (2012), namely that phase intervals of high streak strength and skin-friction increase are associated with high, slowly varying Stokes strain at the level at which the streaks reside, while phase intervals of skin-friction decrease and low streak strength are associated with rapidly varying, low Stokes strain at the same level. Coupled with results derived from GOP theory, this scenario goes some way towards explaining the drag-reduction process. However, if attention is focused on the region closer to the wall, this turns out to be only one leg of a two-legged set of interactions. Specifically, the examination of turbulence properties in phase/wall-normal-space diagrams reveals the following features, thus leading to the following related conclusions:

(i) The phase-wise variations in drag and turbulence within any one actuation cycle display a distinctive hysteresis, wherein the drag-reduction phase extends over a longer proportion of the cycle than the subsequent drag increase. The hysteresis applies to all turbulence properties: their decrease and recovery during the actuation cycle proceed along different paths.

(ii) The hysteresis is attributed to the disruptive influence of the near-wall velocity skewness, which dominates only one portion of the actuation cycle, thus

introducing a pronounced asymmetry in the structure of the Stokes motion during the cycle. When this skewness is high, the turbulence-generation mechanism near the wall is disrupted, the streaks weaken and this contributes to the decrease in drag. When the skewness reduces, turbulence recovers, this recovery occurring predominantly as a consequence of the elevated, lingering Stokes strain in the upper portion of the viscous sublayer. This recovery is inhibited if the period available to this phase is lower than the streak-generation time scale. In this case, the overall effect is a reduction in drag towards an equilibrium low-drag state.

(iii) The budgets show that the variations in the Reynolds stresses during both drag-decrease and -increase phases are driven primarily by fluctuations in production which are balanced mainly by pressure–velocity interaction. In contrast, the dissipation plays a subordinate role. Indeed, in the case of the shear stress, the dissipation is insignificant throughout the actuation cycle. This leads to the conclusion that rising dissipation is not the cause of drag reduction.

(iv) Fluctuations in dissipation and enstrophy correspond closely. Both are observed to decrease when the drag reduces and to rise when the drag increases. This applies not only to fluctuations around the low-drag state, but also to the transient phase.

(v) The phase-wise variations in the enstrophy components show that the streamwise and wall-normal components vary in harmony with the skin-friction and turbulent-stress variations. Both decrease when turbulence is weakened by the Stokes strain and both increase when the Stokes strain is weak. Peaks in the wall-normal enstrophy components correspond to high streak strength due to streak amplification. The spanwise enstrophy component shows a behaviour that is opposite to that of the other two components. This is explained by the fact that the Stokes strain (or rather skewing) causes tilting in the vortices, which then translates to a transfer of enstrophy between the wall-normal and the spanwise components.

Acknowledgement

The authors acknowledge the financial support provided by the UK academic funding agency EPSRC, through grant EP/G061556/1, EADS UK Limited and Airbus Operations Limited. The simulations were performed on the UK's National HPC facility HECToR, as part of the aforementioned EPSRC grant and with additional resources provided by the EPSRC-funded UK Turbulence Consortium.

REFERENCES

BLESBOIS, O., CHERNYSHENKO, S. I., TOUBER, E. & LESCHZINER, M. A. 2013 Pattern prediction by linear analysis of turbulent flow with drag reduction by wall oscillation. *J. Fluid Mech.* **724**, 607–641.

CHOI, K. S. 2002 Near-wall structure of turbulent boundary layer with spanwise-wall oscillation. *Phys. Fluids* **14**, 2530–2542.

DI CICCA, G. M., IUSO, G., SPAZZINI, P. G. & ONORATO, M. 2002 Particle image velocimetry investigation of a turbulent boundary layer manipulated by spanwise wall oscillations. *J. Fluid Mech.* **467**, 41–56.

FISHPOOL, G. M. & LESCHZINER, M. A. 2009 Stability bounds for explicit fractional-step schemes for the Navier–Stokes equations at high Reynolds number. *Comput. Fluids* **38**, 1289–1298.

HOYAS, S. & JIMÉNEZ, J. 2008 Reynolds number effects on the Reynolds-stress budgets in turbulent channels. *Phys. Fluids* **20** (10), 101511.

HUANG, N. E., SHEN, Z., LONG, S. R., WU, M. C., SHIH, H. H., ZHENG, Q., YEN, N.-C., TUNG, C. C. & LIU, H. H. 1998 The empirical mode decomposition and the Hilbert spectrum for nonlinear and non-stationary time series analysis. *Proc. R. Soc. Lond.* A **454** (1971), 903–995.

HUTCHINS, N., MONTY, J. P., GANAPATHISUBRAMANI, B., NG, H. C. H. & MARUSIC, I. 2011 Three-dimensional conditional structure of a high-Reynolds-number turbulent boundary layer. *J. Fluid Mech.* **673**, 255–285.

LARDEAU, S. & LESCHZINER, M. A. 2013 The streamwise drag-reduction response of a boundary layer subjected to a sudden imposition of transverse oscillatory wall motion. *Phys. Fluids* **25** (7), 075109.

MARUSIC, I., MATHIS, R. & HUTCHINS, N. 2010 Predictive model for wall-bounded turbulent flow. *Science* **329** (5988), 193–196.

MOSER, R. D., KIM, J. & MANSOUR, N. N. 1999 Direct numerical simulation of turbulent channel flow up to $\mathrm{Re}_\tau = 590$. *Phys. Fluids* **11** (4), 943–945.

QUADRIO, M. & RICCO, P 2003 Initial response of a turbulent channel flow to spanwise oscillation of the walls. *J. Turbul.* **4** (7).

QUADRIO, M. & RICCO, P. 2004 Critical assessment of turbulent drag reduction through spanwise wall oscillations. *J. Fluid Mech.* **521**, 251–271.

QUADRIO, M., RICCO, P. & VIOTTI, C. 2009 Streamwise-travelling waves of spanwise wall velocity for turbulent drag reduction. *J. Fluid Mech.* **627**, 161–178.

RHIE, C. M. & CHOW, W. L. 1983 Numerical study of the turbulent flow past an airfoil with trailing edge separation. *AIAA J.* **21** (11), 1525–1532.

RICCO, P. 2004 Modification of near-wall turbulence due to spanwise wall oscillations. *J. Turbul.* **5** (24).

RICCO, P., OTTONELLI, C., HASEGAWA, Y. & QUADRIO, M. 2012 Changes in turbulent dissipation in a channel flow with oscillating walls. *J. Fluid Mech.* **700**, 1–28.

RICCO, P. & QUADRIO, M. 2008 Wall-oscillation conditions for drag reduction in turbulent channel flow. *J. Heat Transfer Fluid Flow* **29** (4), 891–902.

SKOTE, M. 2011 Turbulent boundary layer flow subject to streamwise oscillation of spanwise wall-velocity. *Phys. Fluids* **23**, 081703.

SKOTE, M. 2012 Temporal and spatial transients in turbulent boundary layer flow over an oscillating wall. *J. Heat Transfer Fluid Flow* **38**, 1–12.

SKOTE, M. 2013 Comparison between spatial and temporal wall oscillations in turbulent boundary layer flows. *J. Fluid Mech.* **730**, 273–294.

TEMMERMAN, L., LESCHZINER, M. A., MELLEN, C. P. & FRÖHLICH, J. 2003 Investigation of wall-function approximations and subgrid-scale models in large eddy simulation of separated flow in a channel with streamwise periodic constrictions. *Intl J. Heat Fluid Flow* **24** (2), 157–180.

TOUBER, E. & LESCHZINER, M. A. 2012 Near-wall streak modification by spanwise oscillatory wall motion and drag-reduction mechanisms. *J. Fluid Mech.* **693**, 150–200.

XU, C.-X. & HUANG, W.-X. 2005 Transient response of Reynolds stress transport to spanwise wall oscillation in a turbulent channel flow. *Phys. Fluids* **17**, 018101.

YUDHISTIRA, I. & SKOTE, M. 2011 Direct numerical simulation of a turbulent boundary layer over an oscillating wall. *J. Turbul.* **9** (12).